J. Fluid Mech. (2009), *vol.* 624, *pp.* 361–388.
doi:10.1017/S0022112008005405 Printed in the United Kingdom

The effect of Brownian motion on the stability of sedimenting suspensions of polarizable rods in an electric field

BRENDAN D. HOFFMAN[1] AND ERIC S. G. SHAQFEH[1,2]†

[1]Department of Chemical Engineering, Stanford University, Stanford, CA 94305-5025, USA

[2]Department of Mechanical Engineering, Stanford University, Stanford, CA 94305-3030, USA

(Received 9 April 2008 and in revised form 12 November 2008)

We examine the collective dynamics of polarizable, Brownian, sedimenting rods of high aspect ratio. Previous work of Koch and Shaqfeh (*J. Fluids Mech.*, vol. 209, 1989 pp. 521–542) has shown that in the absence of Brownian motion, sedimenting suspensions of rods are unstable to concentration fluctuations and form dense streamers via interparticle hydrodynamic interactions. Recently, Saintillan, Shaqfeh & Darve (*Phys. Fluids*, vol. 18 (121701), 2006*b* p. 1) demonstrated that electric fields can act to stabilize these non-Brownian suspensions of polarizable rods through induced-charge electrokinetic rotation, which forces particle alignment. In this paper, we employ a mean-field linear stability analysis as well as Brownian dynamics simulations to study the effect of thermal motion on the onset of instability. We find that in the absence of electric fields, Brownian motion consistently suppresses instability formation through randomization of particle orientation. However, when electric fields are applied, thermal motion can act to induce instability by counteracting the stabilizing effect of induced-charge orientation.

1. Introduction

Due to the long-range multi-body interactions characterizing low Reynolds number particulate sedimentation, complex collective phenomena frequently arise and are in general poorly understood. Suspensions of orientable particles are of particular interest because they exhibit physics inherently different than those of sphere suspensions. Specifically, when sedimenting under a gravitational field, initially isotropic suspensions of rigid rod-like particles are unstable to concentration fluctuations, and thus dense clusters of particles grow as a consequence of long-range hydrodynamic interactions. This instability was first predicted in a paper by Koch & Shaqfeh (1989), in which they describe the instability mechanism. In short, due to hydrodynamic interactions between rods, dense clusters will sediment faster than less-dense clusters, creating a hydrodynamic disturbance between regions of differing density. This disturbance creates a hydrodynamic torque such that it orients particles in the less-dense regions towards the denser cluster. As the particles sediment, these oriented particles fall towards the regions of higher concentration, amplifying the perturbation. Koch and Shaqfeh mathematically described this phenomenon using a linear stability analysis

---

† Email address for correspondence: esgs@stanford.edu

and mean field theory and showed that horizontal wave perturbations are unstable for sufficiently large container size, and become increasingly unstable with wavelength.

Although experimental evidence of the instability formation exists (see, for instance, the work of Herzhaft & Guazzelli 1999) there are a number of differing qualitative characteristics between the experimental observation and the cluster formation predicted by the theory of Koch and Shaqfeh. For instance, contrary to what is seen in experiments, the stability analysis implies a single dense streamer on the scale of the container width and velocity fluctuations that diverge on the same length scale. In fact, experimental observation of sedimentation reveals the presence of multiple streamers and bounded fluctuations, indicating that additional physics is needed to supplement the original analysis. Saintillan *et al.* have recently attempted to resolve the differences between theory and experiment by examining the effect of stratification (Santillian, Darve & Shaqfeh 2006*a*) and container walls (Saintillan, Darve & Shaqfeh 2006*a*) on suspension stability and cluster formation. They find that stratification and wall effects induce a wavenumber selection that results in multiple streamers for a fixed container size.

There has recently been much interest in controlling suspension microstructure using externally applied electric fields (Saville 1977; Smith *et al.* 2000; Chen *et al.* 2001; Rose *et al.* 2007). Because polarizable rod-like particles suspended in an electrolyte tend to align with an electric field, at sufficient field strengths they are able to resist the hydrodynamic torque created by density fluctuations during sedimentation, and thus the suspension can be stabilized. This stabilization was studied by Saintillan, Shaqfeh & Darve (2006*b*), who concluded that a suspension will indeed stabilize, i.e. concentration fluctuations will not amplify, when the rotational velocities induced by the instability mechanism are balanced by the electrokinetically induced rotation. Saintillan's stability analysis, however, neglects the effects of Brownian motion that becomes an important phenomenon at colloidal length scales.

Recent advances in biological detection applications using functionalized submicrometer metallic bar codes (see Nicewater-Pena *et al.* 2001) (to identify a sequence-specific hybridization, for instance) has heightened interest in examining colloidal rod suspensions. For example, Rose *et al.* (2007) developed analytical models and performed experiments to examine the translation and rotation of polarizable rods in electric fields. Their work, however, considers isolated particles and neglects collective effects. These collective phenomena include hydrodynamic interactions, suspension stability to concentration fluctuations, Brownian motion and coupled electrokinetics. Thus, to fully understand suspension behaviour, one must revisit the stability analysis to include the coupled effects of Brownian motion and electrokinetic rotation.

Herein we will use a linear stability analysis similar to that of Saintillan, Shaqfeh & Darve, combined with Brownian dynamics simulation, to evaluate the effect of these collective phenomena on suspension stability. In the remainder of § 1 we describe past work on induced charge electrokinetics and fibre dynamics. We then proceed to develop the linear stability analysis in § 2 and outline the simulation procedure in § 3. In § 4, we present the results of our analysis and discuss their implications.

1.1. *Induced charge electrokinetic phenomenon*

Squires & Bazant (2004) developed the framework for describing the electrokinetic phenomena related to polarizable particles or surfaces in contact with electrolytes. When subjected to an applied electric field, the charge induced on a solid surface causes a migration of counter-ions, resulting in the formation of an electric double layer (EDL). The time scale for the polarization of the double layer is $\tau_p = \epsilon L/(\sigma \lambda_D)$, where σ is the conductivity of the suspending medium, and is typically of the order of 10^{-6} s (Rose *et al.* 2007). The applied electric field then exerts a force on the charge layer, generating a flow relative to the solid surface. When characterizing a fixed surface, this phenomenon is known as induced-charge electro-osmosis (ICEO), but is alternatively described as induced-charge electrophoresis (ICEP) when characterizing a particle that is mobile in the electrolytic medium. The size of the diffuse charge layer surrounding the surface in a symmetric electrolyte is given by the Debye length

$$\lambda_D = \sqrt{\frac{\epsilon k_B T}{2 n_0 (ze)^2}},$$

where ϵ is the dielectric permittivity of the solution, $k_B T$ is the thermal energy, n_0 is the bulk ion concentration and ze is the charge of a disassociated ion. If the Debye screening length is sufficiently small, one can approximate the net fluid motion at the edge of the EDL as a 'slip' velocity modelled by the Helmholtz–Smoluchowski equation that relates the surface slip to the potential drop across the EDL ζ, the fluid viscosity μ and the component of the electric field $\boldsymbol{E}$ in the direction $\boldsymbol{t}$ tangent to the surface:

$$\boldsymbol{u}_S = -\frac{\epsilon \zeta}{\mu} (\boldsymbol{E} \cdot \boldsymbol{t}) \boldsymbol{t}.$$

Determination of the slip velocity $\boldsymbol{u}_S$ via the calculation of the zeta potential provides the coupling between the equations governing the electric potential and those describing fluid flow. As shown by Squires & Bazant (2005) and Fair & Anderson (1989), the electric potential within the electrolyte volume V must satisfy Laplace's equation

$$\nabla^2 \phi = 0 \qquad \boldsymbol{r} \in V$$

with the boundary conditions at the EDL edge Γ that express no ion current into the surface and the decay of the electric field to the background applied field $\boldsymbol{E}_\infty$:

$$\begin{aligned} n \cdot \nabla \phi &= 0 \qquad \boldsymbol{r} \in \Gamma, \\ -\nabla \phi &\to \boldsymbol{E}_\infty \qquad \boldsymbol{r} \to \infty. \end{aligned}$$

Once the electric potential is known, the zeta potential is obtained as $\zeta(\boldsymbol{r}) = \phi_0 - \phi(\boldsymbol{r})$, where ϕ_0 is the native surface potential.

Santillian, Darve & Shaqfeh (2006*b*) solved the electric problem and slip flow problem analytically for prolate spheroids of aspect ratio A using the method of singularities found in Chwang & Wu (1974) and Han & Yang (1996). They found that for particles oriented in the direction $\boldsymbol{p}$ with no native surface potential, the surface slip velocity as given by the Helmholtz–Smoluchowski equation may be written as

$$\boldsymbol{u}_S(\boldsymbol{r}) = -\frac{\epsilon}{\mu} (\boldsymbol{r} \cdot \mathbf{G}(\boldsymbol{p}) \cdot \boldsymbol{E}_\infty) [(\boldsymbol{I} - \boldsymbol{nn}) \cdot \mathbf{G}(\boldsymbol{p}) \cdot \boldsymbol{E}_\infty],$$

where $\mathbf{G}$ is a geometric tensor that depends on the particle aspect ratio and $\boldsymbol{n}$ is a unit vector normal to the spheroid surface. $\mathbf{G}$ is given by (see Santillan *et al.* 2006*b*)

$$\mathbf{G}(\boldsymbol{p}) = G_\parallel \boldsymbol{pp} + G_\perp (\boldsymbol{I} - \boldsymbol{pp}), \tag{1.1}$$

$$G_{\parallel/\perp} = -4\beta_{\parallel/\perp} \frac{(A^2 - 1)^{3/2}}{A}, \tag{1.2}$$

$$\beta_{\parallel} = \left[-4A(A^2-1)^{1/2} + 2\ln\left(\frac{A+(A^2-1)^{1/2}}{A-(A^2-1)^{1/2}}\right)\right]^{-1}, \tag{1.3}$$

$$\beta_{\perp} = -\left[\frac{4(A^2-1)^{3/2}}{A} - 2A(A^2-1)^{1/2} + \ln\left(\frac{A+(A^2-1)^{1/2}}{A-(A^2-1)^{1/2}}\right)\right]^{-1}. \tag{1.4}$$

1.2. *Fibre dynamics*

In this work, we consider the sedimentation dynamics of axisymmetric slender particles of length $2L$ and diameter $2b$ (aspect ratio $A = L/b$) suspended in a fluid of viscosity μ. Each particle's position and orientation may be described in terms of a centre of mass position $\boldsymbol{x}$ and director vector $\boldsymbol{p}$. For large aspect ratios, the motion of each particle is described by a modified slender-body theory of Batchelor (1970) Santillan *et al.* (2006*b*), which, to $\mathcal{O}(1/\ln(2A))$, relates the centre of mass and rotational velocities $\dot{\boldsymbol{x}}$ and $\dot{\boldsymbol{p}}$ to a distribution of Stokeslets $\boldsymbol{f}$ along the particle length parametrized by $s \in [-L, L]$:

$$\dot{\boldsymbol{x}} + s\dot{\boldsymbol{p}} - \boldsymbol{u}_D(\boldsymbol{x}+\boldsymbol{p}s) + \overline{\boldsymbol{u}_S}(s) = \frac{\ln(2A)}{4\pi\mu}(\boldsymbol{I}+\boldsymbol{pp})\boldsymbol{\cdot}\boldsymbol{f}(s). \tag{1.5}$$

In the above equation, $\boldsymbol{u}_D$ is the net hydrodynamic disturbance velocity acting at the point $\boldsymbol{x}+\boldsymbol{p}s$ due to the motion of all other fibres in the suspension, and $\overline{\boldsymbol{u}_S}$ is the linearized slip velocity averaged across a particle's cross-section. $\overline{\boldsymbol{u}_S}$ is given by Saintillan *et al.* (2006*d*) to $\mathcal{O}(A^{-2})$ as

$$\overline{\boldsymbol{u}_S}(s) = -\frac{\epsilon}{\mu}s(\boldsymbol{p}\boldsymbol{\cdot}\boldsymbol{G}'\boldsymbol{\cdot}\boldsymbol{E}_\infty)\boldsymbol{G}'\boldsymbol{\cdot}\boldsymbol{E}_\infty, \tag{1.6}$$

where $\boldsymbol{G}' = G_{\parallel}\boldsymbol{pp} + 1/2G_{\perp}(\boldsymbol{I}-\boldsymbol{pp})$.

The integral of (1.5) over the fibre length relates the centre of mass velocity to the net force on the particle $\boldsymbol{F} = \int_{-L}^{L}\boldsymbol{f}(s)\,\mathrm{d}s$

$$\dot{\boldsymbol{x}} = \frac{1}{2L}\int_{-L}^{L}\boldsymbol{u}_D(\boldsymbol{x}+\boldsymbol{p}s)\,\mathrm{d}s + \frac{\ln(2A)}{8\pi\mu L}(\boldsymbol{I}+\boldsymbol{pp})\boldsymbol{\cdot}\boldsymbol{F}, \tag{1.7}$$

while the integral of the cross product of (1.5) with $\boldsymbol{p}$ yields an equation for the rotational velocity in terms of the net applied torque $\boldsymbol{T} = \int_{-L}^{L} s\boldsymbol{p}\wedge\boldsymbol{f}(s)\,\mathrm{d}s$

$$\dot{\boldsymbol{p}} = \frac{3}{2L^3}(\boldsymbol{I}-\boldsymbol{pp})\boldsymbol{\cdot}\int_{-L}^{L}[\boldsymbol{u}_D(\boldsymbol{x}+\boldsymbol{p}s) - \overline{\boldsymbol{u}_S}(s)]s\,\mathrm{d}s - \frac{3\ln(2A)}{8\pi\mu L^3}\boldsymbol{p}\wedge\boldsymbol{T}. \tag{1.8}$$

For axisymmetric particles sedimenting under gravity, the total force $\boldsymbol{F}$ consists of a gravitational component $\boldsymbol{F}_g$ and a Brownian component $\boldsymbol{F}_B$. There is no net electrokinetic force due to symmetry. The total torque consists of a small electro-rotational torque that is neglected (see Santillan *et al.* 2006*b*) and the Brownian torque $\boldsymbol{T}_B$. The hydrodynamic disturbance $\boldsymbol{u}_D$ at any point in the fluid $\boldsymbol{r}$ is given by the net flow due to the Stokeslet distributions along each of the N fibres,

$$\boldsymbol{u}_D(\boldsymbol{r}) = \frac{1}{8\pi\mu}\sum_{j=1}^{N}\int_{-L}^{L}\boldsymbol{J}(\boldsymbol{r}-\boldsymbol{x}_j-s\boldsymbol{p}_j)\boldsymbol{\cdot}\boldsymbol{f}_j(s)\,\mathrm{d}s,$$

where $\boldsymbol{J}$ is the appropriate Green's function of the Stokes equations, which depends on the geometry of the suspension boundaries. The solution to this set of equations for each fibre in the suspension fully describes the evolution of the microstructure for slender bodies.

2. Mean field theory and stability analysis

We now develop a mean field theory that describes the suspension as a continuum for the purpose of a linear stability analysis. We begin the linear stability analysis with the particle conservation equation, which describes the evolution of the particle density field $c(\boldsymbol{x}, \boldsymbol{p}, t)$, where $\iint c\,\mathrm{d}\boldsymbol{p}\,\mathrm{d}\boldsymbol{V} = N_p$, the number of particles. Neglecting hydrodynamic corrections in the rotational (d_r) and centre of mass ($\boldsymbol{D}$) diffusivities, the conservation equation is

$$\frac{\partial c}{\partial t} + \nabla_{\boldsymbol{p}} \cdot (\dot{\boldsymbol{p}} c) + \nabla_{\boldsymbol{x}} \cdot (\dot{\boldsymbol{x}} c) - d_r \nabla_{\boldsymbol{p}}^2 c - \nabla_{\boldsymbol{x}} \cdot \boldsymbol{D} \cdot \nabla_{\boldsymbol{x}} c = 0. \tag{2.1}$$

where the $\dot{\boldsymbol{p}}$ and $\dot{\boldsymbol{x}}$ arise from the deterministic portions of (1.7) and (1.8) (i.e. neglecting the Brownian force and torque). For a long, slender rod with aspect ratio A, the single-particle diffusivities are given by slender-body theory to $\mathcal{O}(\ln(2A)^{-1})$ as (Kim & Karrila 1991; Larson 1999)

$$d_r = \frac{3k_B T \ln(2A)}{8\pi\mu L^3}, \qquad \boldsymbol{D} = \frac{k_B T \ln(2A)}{8\pi\mu L}\left[\boldsymbol{I} + \boldsymbol{p}\boldsymbol{p}\right].$$

Following Koch & Shaqfeh (1989) and Saintllian *et al.* (2006*a*), hydrodynamic interactions between particles are captured through a mean field approximation to the point-particle Stokes equation, in which a disturbance flow is driven by a gravitational body force through a spatially varying local density:

$$-\mu\nabla^2 \boldsymbol{u} + \nabla p = \boldsymbol{F}_g \int c\,\mathrm{d}\boldsymbol{p}. \tag{2.2}$$

The stress coupling terms arising from ICEP, Brownian motion and extra hydrodynamic stress due to the particle rigidity have been deliberately omitted from (2.2), as the instability mechanism arises solely from the buoyant force coupling between concentration perturbations and the mean flow field. Additionally, it can be shown that in dilute solutions, the induced rotation of a particle external to that of buoyancy coupling is dominated by the electrophoretic slip velocity, while the rotation induced by the ICEP hydrodynamics from neighbouring particles decays as r^{-3}. Because the key mechanism of the concentration instability arises from particle rotation towards regions of higher density, we shall only consider the primary rotational effect of ICEP while neglecting its hydrodynamic coupling. We expect the additional neglected stresses will bring about a local viscosity increase in the regions of high density but will not significantly alter the onset of instability.

Within the point particle approximation, a fibre's translational velocity is taken as the sum of its dilute sedimentation velocity and the net disturbance velocity evaluated at its centre of mass: $\dot{\boldsymbol{x}} = \boldsymbol{U}_s + \boldsymbol{u}(\boldsymbol{x})$, where $\boldsymbol{U}_s = \ln(2A)/8\pi\mu L(\boldsymbol{I} + \boldsymbol{p}\boldsymbol{p})\boldsymbol{F}_g$ for a slender particle. The rotational velocity has contributions from both the electrophoretic slip velocity and the local disturbance flow in the fluid. Assuming a linear disturbance velocity gradient $\nabla\boldsymbol{u}$ on the scale of the particle length, the rotational velocity is given by a modified Jeffery's equation:

$$\dot{\boldsymbol{p}} = \dot{\boldsymbol{p}}_{ICEP} + (\boldsymbol{I} - \boldsymbol{p}\boldsymbol{p}) \cdot \boldsymbol{E}(\boldsymbol{x}) \cdot \boldsymbol{p} + \boldsymbol{\Omega}(\boldsymbol{x}) \cdot \boldsymbol{p}, \tag{2.3}$$

where $\boldsymbol{E}$ and $\boldsymbol{\Omega}$ are the symmetric and antisymmetric parts of $\nabla\boldsymbol{u}$, respectively, and $\dot{\boldsymbol{p}}_{ICEP}$ is obtained by integrating the term in (1.6) corresponding to the electrophoretic slip:

$$\dot{\boldsymbol{p}}_{ICEP} = \frac{\epsilon G_\parallel G_\perp}{2\mu}(\boldsymbol{p} \cdot E_\infty)(\boldsymbol{I} - \boldsymbol{p}\boldsymbol{p}) \cdot \boldsymbol{E}_\infty.$$

We take as our base state a spatially homogeneous dispersion that satisfies the concentration evolution equation, $c = n\Psi(\boldsymbol{p})$, where n is the suspension average number density of particles and Ψ is only a function of orientation. The base state drives no net disturbance velocity, so $\boldsymbol{u} = 0$, and $\dot{\boldsymbol{p}} = \dot{\boldsymbol{p}}_{ICEP}$. The steady solution for Ψ is given by (Santillan *et al.* 2006*d*)

$$\Psi(\phi) = N \exp\left[\frac{\pi L^3 \epsilon E_\infty^2}{3k_B T \ln(2A)} G_{||} G_\perp \cos(2\phi)\right], \tag{2.4}$$

where ϕ is the angle between the particle's orientation vector $\boldsymbol{p}$ and the electric field, and N is a constant of normalization such that $\int \Psi \,\mathrm{d}\boldsymbol{p} = 1$. For dilute conditions in the absence of electric fields, $\Psi = (4\pi)^{-1}$, and the suspension is isotropically oriented.

To conduct the linear stability analysis, we introduce a density perturbation of wave-vector $\boldsymbol{k}$ and (small) magnitude δ into (2.1) of the form $c = n\Psi + n\delta\tilde{c}(\boldsymbol{k}, \omega, \boldsymbol{p})\mathrm{e}^{\mathrm{i}(\boldsymbol{k}\cdot\boldsymbol{x} - \omega t)}$. As in previous work (Koch & Shaqfeh 1989; Santillan *et al.* 2006*b*), only horizontal plane-waves (i.e. the most unstable waves) are considered such that $\boldsymbol{k}\cdot\hat{\boldsymbol{z}} = 0$ and $\hat{\boldsymbol{z}}$ is a unit vector in the direction of gravity. The growth rate ω will determine the stability of the suspension to this perturbation, and will be obtained as the solution to an eigenvalue problem. The induced perturbation drives a disturbance flow given by (Hasimoto 1958)

$$\boldsymbol{u} = n\delta \frac{\mathrm{e}^{-\mathrm{i}\omega t}}{\mu k^2}\left(\boldsymbol{I} - \frac{\boldsymbol{k}\boldsymbol{k}}{k^2}\right)\cdot \boldsymbol{F}_g \int \tilde{c}\,\mathrm{d}\boldsymbol{p}. \tag{2.5}$$

The gradient of (2.5) drives fibre rotation, and from (2.3) the rotational velocity becomes

$$\left.\begin{aligned} \dot{\boldsymbol{p}} &= \dot{\boldsymbol{p}}_{ICEP} + n\delta \mathrm{e}^{\mathrm{i}\boldsymbol{k}\cdot\boldsymbol{x} - \mathrm{i}\omega t}\dot{\boldsymbol{p}}_{DIST} \\ \dot{\boldsymbol{p}}_{DIST} &= \frac{i}{\mu k^2}(\boldsymbol{p}\cdot\boldsymbol{k})(\boldsymbol{I} - \boldsymbol{p}\boldsymbol{p})\left(\boldsymbol{I} - \frac{\boldsymbol{k}\boldsymbol{k}}{k^2}\right)\cdot\boldsymbol{F}_g\int \tilde{c}\,\mathrm{d}\boldsymbol{p}. \end{aligned}\right\} \tag{2.6}$$

Substituting c, $\dot{\boldsymbol{p}}$ and $\dot{\boldsymbol{x}}$ into the conservation equation, subtracting off the base state equation for $\tilde{c}$, and keeping terms to $\mathcal{O}(\delta)$ yields an integro-differential eigenvalue equation for ω,

$$-i\omega\tilde{c} + \nabla_{\boldsymbol{p}}\cdot(\tilde{c}\dot{\boldsymbol{p}}_{ICEP}) + n\nabla_{\boldsymbol{p}}\cdot(\Psi\dot{\boldsymbol{p}}_{DIST}) + i\boldsymbol{k}\cdot\boldsymbol{U}_s\tilde{c} - d_r\nabla_{\boldsymbol{p}}^2\tilde{c} + \boldsymbol{k}\cdot\boldsymbol{D}\cdot\boldsymbol{k}\tilde{c} = 0, \tag{2.7}$$

where a complete description of (2.7) requires the following relations:

$$\nabla_{\boldsymbol{p}}\cdot\dot{\boldsymbol{p}}_{ICEP} = \frac{\epsilon G_{||} G_\perp E_\infty^2}{2\mu}\boldsymbol{e}_\infty\cdot(\boldsymbol{I} - 3\boldsymbol{p}\boldsymbol{p})\cdot\boldsymbol{e}_\infty, \tag{2.8}$$

$$\nabla_{\boldsymbol{p}}\cdot\dot{\boldsymbol{p}}_{DIST} = \frac{-3i}{\mu k^2}(\boldsymbol{p}\cdot\boldsymbol{k})\boldsymbol{p}\cdot\left(\boldsymbol{I} - \frac{\boldsymbol{k}\boldsymbol{k}}{k^2}\right)\cdot\boldsymbol{F}_g\int\tilde{c}\,\mathrm{d}\boldsymbol{p}, \tag{2.9}$$

$$\nabla_{\boldsymbol{p}}\Psi = h(\boldsymbol{p})(\boldsymbol{I} - \boldsymbol{p}\boldsymbol{p})\cdot\boldsymbol{e}_\infty, \tag{2.10}$$

$$h(\boldsymbol{p}) = N\frac{4\pi L^3\epsilon E_\infty^2}{3k_B T\ln(2A)}(\boldsymbol{p}\cdot\boldsymbol{e}_\infty)\exp\left\{\frac{\pi L^3\epsilon E_\infty^2}{3k_B T\ln(2A)}G_{||}G_\perp\cos(2\phi)\right\}, \tag{2.11}$$

and where $|\boldsymbol{E}_\infty|\boldsymbol{e}_\infty = \boldsymbol{E}_\infty$. Equations (2.7) and (2.11) are then non-dimensionalized using the length scale $l_c = 2L$, the total particle length, and a sedimentation time scale $t_s = 8\pi\mu L^2/|F_g|\ln(2A)$, the time for a particle aligned with gravity to sediment its length. After substitution and manipulation, (2.7) becomes

$$
\begin{aligned}
0 = &-i\omega\tilde{c} + \frac{i\beta\Psi}{k^2}(\boldsymbol{p}\cdot\hat{\boldsymbol{z}})(\boldsymbol{p}\cdot\boldsymbol{k})\int \tilde{c}\,\mathrm{d}\boldsymbol{p} \\
&+\frac{1}{2}HG_{\|}G_{\perp}\left\{\left[1-3(\boldsymbol{p}\cdot\boldsymbol{e}_{\infty})^2\right]\tilde{c} + (\boldsymbol{p}\cdot\boldsymbol{e}_{\infty})\boldsymbol{e}_{\infty}\cdot\nabla_{\boldsymbol{p}}\tilde{c}\right\} \\
&-\frac{i\beta h(\boldsymbol{p})}{3k^2}(\boldsymbol{p}\cdot\boldsymbol{k})\left[(\boldsymbol{e}_{\infty}\cdot\hat{\boldsymbol{z}}) - (\boldsymbol{p}\cdot\boldsymbol{e}_{\infty})(\boldsymbol{p}\cdot\hat{\boldsymbol{z}})\right]\int \tilde{c}\,\mathrm{d}\boldsymbol{p} \\
&-\frac{i}{2}(\boldsymbol{p}\cdot\boldsymbol{k})(\boldsymbol{p}\cdot\hat{\boldsymbol{z}})\tilde{c} - 3Pe^{-1}\nabla_{\boldsymbol{p}}^2\tilde{c} + \frac{1}{4}Pe^{-1}\left[k^2 + (\boldsymbol{p}\cdot\boldsymbol{k})^2\right]\tilde{c}, \qquad (2.12)
\end{aligned}
$$

where we have used $\boldsymbol{k}\cdot\boldsymbol{F}_g = -|\boldsymbol{F}_g|\boldsymbol{k}\cdot\hat{\boldsymbol{z}} = \boldsymbol{0}$ and defined the following dimensionless constants:

$$
\left.
\begin{aligned}
\beta &= \frac{6\pi}{\ln(2A)}nl_c^3, \\
H &= \frac{8\pi L^2\epsilon E_{\infty}^2}{|\boldsymbol{F}_g|\ln(2A)}, \\
Pe^{-1} &= \frac{k_BT}{|\boldsymbol{F}_g|L}.
\end{aligned}
\right\} \qquad (2.13)
$$

Each constant defined above has an important physical meaning. The constant β is essentially a dimensionless concentration parameter, H represents the ratio between induced electrokinetic rotation and buoyancy forces, and the inverse Péclet number Pe^{-1} describes the relative importance of thermal motion and gravity. The role of gravity or buoyancy in both H and Pe^{-1} is to represent the mechanism for instability formation through sedimentation-driven hydrodynamic interactions. For example, to examine solely the effect of varying electric field strength on suspension stability, one would vary H at fixed Pe^{-1} and β.

For simplicity in the following sections, we will consider only electric fields oriented in the direction of gravity, $\boldsymbol{e}_{\infty} = \hat{\boldsymbol{z}}$, and heretofore all equations will be presented in a dimensionless form.

2.1. *No electric field: perturbation solution*

We begin the stability solution by examining the effect of Brownian motion on suspension stability in the absence of electric fields. The effects of thermal motion will be two-fold; it will act to randomize the rotational velocities of the sedimenting fibres, opposing the hydrodynamic rotation that drives the concentration instability, as well as driving particles from regions of high density (streamers) to regions of low density. Both effects will tend to stabilize the suspension by suppressing streamer growth rates. In the absence of electric fields ($E_{\infty} = 0$), the base orientation state in dilute suspensions is isotropic, $\Psi = (4\pi)^{-1}$. Equation (2.12) therefore becomes

$$
\begin{aligned}
-\mathrm{i}\omega\tilde{c} + \frac{\mathrm{i}\beta}{4\pi k^2}(\boldsymbol{p}\cdot\hat{\boldsymbol{z}})(\boldsymbol{p}\cdot\boldsymbol{k})\int \tilde{c}\,\mathrm{d}\boldsymbol{p} - \frac{\mathrm{i}}{2}(\boldsymbol{p}\cdot\boldsymbol{k})(\boldsymbol{p}\cdot\hat{\boldsymbol{z}})\tilde{c} - 3Pe^{-1}\nabla_{\boldsymbol{p}}^2\tilde{c}& \\
+\frac{1}{4}Pe^{-1}\left[k^2 + (\boldsymbol{p}\cdot\boldsymbol{k})^2\right]\tilde{c} = 0.& \qquad (2.14)
\end{aligned}
$$

For weak thermal motion relative to the gravitational force (corresponding to large fibres), $\tilde{c}$ and ω may be obtained as perturbation expansions in the limit of small Pe^{-1}:

$$
\begin{aligned}
\tilde{c} &= \tilde{c}_0 + Pe^{-1}\tilde{c}_1 + Pe^{-2}\tilde{c}_2 + \cdots \\
\omega &= \omega_0 + Pe^{-1}\omega_1 + Pe^{-2}\omega_2 + \cdots. \qquad (2.15)
\end{aligned}
$$

It should be noted that this perturbation expansion is singular because in the absence of Brownian motion ($Pe^{-1}=0$) we find only a single eigenvalue $\omega^{(1)}$ as opposed to a set of eigenvalues $\{\omega^{(i)}\}$ demanded by (2.14). However, we expect the effect of Brownian motion to be stabilizing and will assume that all eigenvalues neglected by the perturbation solution correspond to stable modes with $\mathrm{Im}(\omega^{(i)})<0$, $i>1$. This assumption will be verified numerically in a subsequent section and only the correction to $\omega^{(1)}$ will be evaluated at present. Substituting (2.15) into (2.14), at $\mathscr{O}(Pe^{0})$ we obtain

$$\left(\omega_0 + \frac{1}{2}(\boldsymbol{p}\cdot\boldsymbol{k})(\boldsymbol{p}\cdot\hat{\boldsymbol{z}})\right)\tilde{c}_0 = \frac{\beta}{4\pi k^2}(\boldsymbol{p}\cdot\hat{\boldsymbol{z}})(\boldsymbol{p}\cdot\boldsymbol{k})\int \tilde{c}_0\,\mathrm{d}\boldsymbol{p}. \tag{2.16}$$

A solvability condition for the eigenvalue ω_0 may be obtained by integrating (2.16) over all particle orientations and discarding the normalization constant $\int \tilde{c}_0\,\mathrm{d}\boldsymbol{p}$:

$$1 = \frac{\beta}{4\pi k^2}\int \frac{(\boldsymbol{p}\cdot\hat{\boldsymbol{z}})(\boldsymbol{p}\cdot\boldsymbol{k})}{(\omega_0+\frac{1}{2}(\boldsymbol{p}\cdot\boldsymbol{k})(\boldsymbol{p}\cdot\hat{\boldsymbol{z}}))}\,\mathrm{d}\boldsymbol{p}. \tag{2.17}$$

The first eigenfunction $\tilde{c}_0$ is given by (2.16) to within a numerical constant. Equation (2.17) can be solved numerically for ω_0 or alternatively, asymptotically evaluated in the limit of small $\boldsymbol{k}$ as done by Saintllian *et al.* (2006*a*), giving

$$\omega_0 = \pm\mathrm{i}\sqrt{\frac{\beta}{30}} - \frac{\mathrm{i}\beta}{1680}\left(\frac{30}{\beta}\right)^{3/2}|\boldsymbol{k}|^2 + \mathscr{O}(|\boldsymbol{k}|^3). \tag{2.18}$$

Defining the functions $f\equiv \mathrm{i}\beta/4\pi k^2(\boldsymbol{p}\cdot\hat{\boldsymbol{z}})(\boldsymbol{p}\cdot\boldsymbol{k})$ and $g\equiv -1/2(\boldsymbol{p}\cdot\boldsymbol{k})(\boldsymbol{p}\cdot\hat{\boldsymbol{z}})$, and the linear operators $\mathscr{L}_0\equiv(\mathrm{i}g/f+\int\mathrm{d}\boldsymbol{p})$ and $\mathscr{L}_1\equiv 1/f(-3\nabla_{\boldsymbol{p}}^2+1/4[k^2+(\boldsymbol{p}\cdot\boldsymbol{k})^2])$, as well as the inner product $\langle\circ,\bar{\bullet}\rangle=\int\circ\bar{\bullet}\,\mathrm{d}\boldsymbol{p}$ (where $\bar{\bullet}$ denotes the complex conjugate of $\bullet$), we can succinctly write the equation describing the first correction ω_1 at $\mathscr{O}(Pe^{-1})$ to the eigenvalue ω as

$$-\mathrm{i}\omega_0\frac{\tilde{c}_1}{f} - \mathrm{i}\omega_1\frac{\tilde{c}_0}{f} + \mathscr{L}_0\tilde{c}_1 + \mathscr{L}_1\tilde{c}_0 = 0. \tag{2.19}$$

To proceed, we take the inner product of each term in (2.19) with $\tilde{c}_0$, giving

$$\left.\begin{aligned}
\langle\mathscr{L}_0\tilde{c}_1,\bar{\tilde{c}}_0\rangle + \langle\mathscr{L}_1\tilde{c}_0,\bar{\tilde{c}}_0\rangle &= \mathrm{i}\omega_0\left\langle\frac{\tilde{c}_1}{f},\bar{\tilde{c}}_0\right\rangle + \mathrm{i}\omega_1\left\langle\frac{\tilde{c}_0}{f},\bar{\tilde{c}}_0\right\rangle\\
\langle\tilde{c}_1,\mathscr{L}_0\bar{\tilde{c}}_0\rangle + \langle\mathscr{L}_1\tilde{c}_0,\bar{\tilde{c}}_0\rangle &=\\
\mathrm{i}\omega_0\left\langle\tilde{c}_1,\frac{\bar{\tilde{c}}_0}{f}\right\rangle + \langle\mathscr{L}_1\tilde{c}_0,\bar{\tilde{c}}_0\rangle &=\\
\langle\mathscr{L}_1\tilde{c}_0,\bar{\tilde{c}}_0\rangle &= \mathrm{i}\omega_1\left\langle\frac{\tilde{c}_0}{f},\bar{\tilde{c}}_0\right\rangle.
\end{aligned}\right\}$$

In the above equation, we have used the fact that the operator $\mathscr{L}_0$ is self-adjoint over the inner-product space defined. The eigenvalue correction ω_1 can then be determined in terms of the known eigenfunction $\tilde{c}_0$ as $\omega_1=-\mathrm{i}\langle\mathscr{L}_1\tilde{c}_0,\bar{\tilde{c}}_0\rangle/\langle\tilde{c}_0/f,\bar{\tilde{c}}_0\rangle$, which for small $|\boldsymbol{k}|$ has the solution

$$\omega_1 = -9\mathrm{i} - \frac{3\mathrm{i}}{7\omega_0^2}|\boldsymbol{k}|^2 - \frac{5\mathrm{i}}{14}|\boldsymbol{k}|^2 + \mathscr{O}(|\boldsymbol{k}|^3). \tag{2.20}$$

From (2.20) it is evident that the first-order effect of Brownian motion is to reduce the growth rate of the instability. The validity of the perturbation solution will be shown in the next section by comparing to our numerical results.

It is instructive to separate the respective contributions from centre of mass and rotational diffusivity for ω_1. As written in (2.20), the first two terms arise from the rotational diffusion, while the third term arises from the centre of mass term. It can therefore be seen that the primary effect of rotational Brownian motion is to reduce the instability growth rate at constant wavenumber by randomizing particle orientations, while the centre of mass diffusion tends to disperse high-frequency density fluctuations by reducing the wavenumber at which the instability appears. At finite Péclet number and for sufficiently small wave-numbers (large wavelengths), centre of mass dispersion alone cannot suppress the onset of instability because particles cannot diffuse away from large regions of higher density as quickly as they are attracted through gravity-driven hydrodynamic interactions.

2.2. *Spectral solution*

While (2.14) permits a solution for weak thermal motion, the additional terms in (2.12) corresponding to ICEP effects render a perturbation strategy impossible. We therefore seek a numerical solution to the eigenvalue set $\{\omega^{(i)}\}$ by expanding the function $\{\tilde{c}^{(i)}\}$ in an appropriate basis set of functions. Because the eigenfunctions of the density disturbance are defined on the unit sphere and are periodic and continuous, we choose the spherical harmonics as our basis set: $\tilde{c} = \sum_{q=0}^{q=\infty} \sum_{s=-q}^{s=q} a_{qs} Y_q^s$. Truncating this expansion at $q = Q$, substituting into (2.12) and taking the inner product with respect to $Y_{q'}^{s'}$ give a discrete representation for the eigenvalue set in terms of a matrix equation, which may be written as $\boldsymbol{M} \cdot \boldsymbol{a} = \omega \boldsymbol{a}$. The eigenvalues of the matrix $\boldsymbol{M}$ are therefore an approximation to the first $(Q+1)^2$ eigenvalues of the set $\{\omega^{(i)}\}$. We present in the Appendix the algebraic details related to the spectral solution. We find, consistent with our previous assumption, that a maximum of one unstable eigenmode ($\mathrm{Im}(\omega^i) < 0$) exists for all values of H and Pe^{-1} examined. Only the first eigenvalue therefore needs to be accurately computed and generally converges with Q at a truncation number of $Q = 30$. As the inverse Péclet is increased, the truncation number necessary for convergence of the first eigenvalue decreases substantially, although in our solutions we always choose $Q > 20$. Convergence is enhanced with increasing Pe^{-1} because the dominance of the spherical Laplacian operator, $\nabla_{\boldsymbol{p}}^2 \tilde{c}$, in the solution of eigenvalue (2.12) increases as well, and the spherical harmonics are eigenfunctions of this operator.

We present in figure 1 the perturbation results derived in the previous section compared to the (converged) spectral solution obtained with 25 harmonics. The perturbation result is clearly useful only for $Pe^{-1} \lesssim 0.02$ and $k^* \lesssim 0.5$. It is useful, however, for determining the first-order effects of Brownian motion on suspension stability. In all subsequent sections the spectral solution will be used unless otherwise noted.

3. Brownian dynamics simulation

3.1. *Base equations for fibre dynamics*

To test the results of the mean field stability analysis and more completely analyse the stability of our system, we have performed Brownian dynamics simulations of a periodic suspension. Our simulations resolve individual fibre dynamics, hydrodynamic interactions between fibres and near-field lubrication interactions. The basis for the simulation begins with the equations presented in § 1.2. We non-dimensionalize these equations using a characteristic length scale $l_c = 2L$, the total fibre length and time scale $t_c = 8\mu L^3/k_B T$, which is proportional to a fibre's rotational diffusivity. Note this differs from the scaling used in the mean field theory and stability analysis because

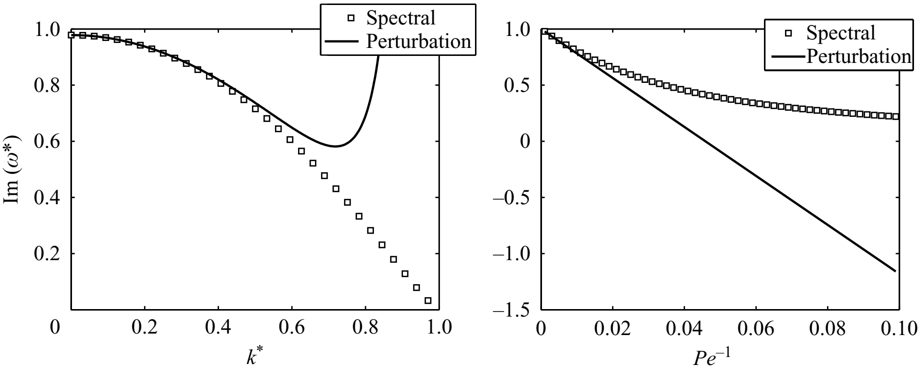

FIGURE 1. Solid line: Perturbation solution for the first eigenvalue corresponding to (2.18) and (2.20) for $nl_c^3 = 1.0$, and $A = 20$. Squares: Spectral solution to the eigenvalue (2.14) using 25 harmonics in the expansion. The left panel shows the growth rate vs. k for a fixed Péclet number of $Pe^{-1} = 10^{-3}$, while the right panel shows the growth rate vs. Peclet number for a fixed $k = 0.001$.

resolution of time scales shorter than the sedimentation time is critical for evaluating the role of Brownian motion on sedimentation stability. Additionally, for typical particle lengths of the order of 1 μm, t_c has a value of the order of 1 s. We may therefore assume that the double layer is completely polarized at all time scales of interest in the simulation.

Using these scalings, the equations describing fibre j's centre of mass and rotational motion become

$$\dot{\boldsymbol{x}}_j = \int_{-1/2}^{1/2} \boldsymbol{v}_D(\boldsymbol{x}_j + \boldsymbol{p}_j s_j)\,\mathrm{d}s_j + \frac{\ln(2A)}{4\pi}(\boldsymbol{I} + \boldsymbol{p}_j\boldsymbol{p}_j)\cdot\mathscr{F}_j \tag{3.1}$$

$$\dot{\boldsymbol{p}}_j = 12(\boldsymbol{I} - \boldsymbol{p}_j\boldsymbol{p}_j)\cdot \int_{-1/2}^{1/2} [\boldsymbol{v}_D(\boldsymbol{x}_j + \boldsymbol{p}_j s_j) - Pe^E \boldsymbol{v}_D(s_j)]s_j\,\mathrm{d}s_j - \frac{3\ln(2A)}{\pi}\boldsymbol{p}_j \wedge \mathscr{T}_j, \tag{3.2}$$

where $\boldsymbol{v}_D$ and $\boldsymbol{v}_S$ are the dimensionless disturbance and circumferentially averaged slip velocities, $\mathscr{F}$ and $\mathscr{T}$ are the dimensionless externally applied force and torque and $\boldsymbol{Pe}^E$ is the electric Péclet number defined as

$$Pe^E = \frac{8L^3\epsilon E_\infty^2}{k_B T} = HPe\frac{\ln(2A)}{\pi}. \tag{3.3}$$

For the sedimentation problem considered, the net (dimensionless) force is a sum of Brownian, lubrication and gravitational forces $\mathscr{F} = \mathscr{F}_B + \mathscr{F}_L + 2Pe\hat{z}$, and any applied torque is solely due to Brownian motion.

3.2. *Hydrodynamic interaction*

3.2.1. *Basic equations*

The disturbance velocity at location $\boldsymbol{r}$ is computed using the modified Green's function of the periodic Stokes equations, $\boldsymbol{J}_p$, given in Hasimoto (1958). Consider an infinite periodic array of point forces with a unit cell of volume V_c, lattice vectors $\{\boldsymbol{a}_i\}$ and reciprocal basis $\{\boldsymbol{b}_i\}$. If the forces are localized at coordinates $\boldsymbol{r}_p + n_1\boldsymbol{a}_1 + n_2\boldsymbol{a}_2 + n_3\boldsymbol{a}_3$, $\boldsymbol{J}_p$ is given in a dimensionless form by

$$\boldsymbol{J}_p(\boldsymbol{r}) = \frac{1}{8\pi}\,[S_1\boldsymbol{I} - \nabla\nabla S_2] \tag{3.4}$$

$$S_1 = \frac{2}{\pi V_c} \sum_{k \neq 0} \frac{e^{-2\pi \mathrm{i} \boldsymbol{k} \cdot (\boldsymbol{r} - \boldsymbol{r}_p)}}{k^2} \tag{3.5}$$

$$S_2 = \frac{-1}{2\pi^3 V_c} \sum_{k \neq 0} \frac{e^{-2\pi \mathrm{i} \boldsymbol{k} \cdot (\boldsymbol{r} - \boldsymbol{r}_p)}}{k^4}, \tag{3.6}$$

where $\boldsymbol{k} = m_1\boldsymbol{b}_1 + m_2\boldsymbol{b}_2 + m_3\boldsymbol{b}_3$. The Green's functions can be evaluated using traditional Ewald sums (Hasimoto 1958) or a smooth mesh algorithm (Saintillan, Darve & Shaqfeh 2005) as described below. The net disturbance at a point on fibre k is then given as

$$\boldsymbol{v}_D(\boldsymbol{x}_k + s_k \boldsymbol{p}_k) = \sum_{j=1}^{N} \int_{-1/2}^{1/2} \boldsymbol{K}(\boldsymbol{x}_k + s_k \boldsymbol{p}_k - \boldsymbol{x}_j - s_j \boldsymbol{p}_j) \cdot \boldsymbol{f}_j(s_j)\, \mathrm{d}s_j \tag{3.7}$$

$$\boldsymbol{K} = \begin{cases} \boldsymbol{J}_p & j \neq k \\ \boldsymbol{J}_p - \boldsymbol{J} & j = k, \end{cases}$$

where the free space Oseen tensor $\boldsymbol{J}$ must be subtracted when $j = k$ to ensure that each fibre interacts with all periodic images, but not itself, as self-interaction is already captured in the slender-body equation for the force density. In the limit as $s_j \rightarrow s_k$, the proper limiting form of the expression $\boldsymbol{J}_p - \boldsymbol{J}$ is used.

To compute the integrals in (3.7), the fibres are discretized with M quadrature points and Gauss–Legendre quadrature is used. These integrals introduce MN additional unknowns, the force distribution at along each fibre evaluated at each quadrature point. To avoid the computational expense associated with additional unknowns, we employ the same force distribution linearization of Harlen, Sundararajkumar & Koch (1999), which was subsequently used in Butler & Shaqfeh (2002) and Saintillan *et al.* (2005). The result of this linearization yields the following for $\boldsymbol{f}(s)$, where for each fibre the M unknowns have been replaced by a single scalar stresslet $\mathscr{S}$:

$$\boldsymbol{f}(s) = \mathscr{F} + 12s(\mathscr{T} \wedge \boldsymbol{p} + \mathscr{S}\boldsymbol{p}). \tag{3.8}$$

The stresslet represents the contribution to the fluid stress due to particle rigidity and must be solved for consistently using the relation (Santillan *et al.* 2006*b*)

$$\mathscr{S}_j = -\frac{2\pi}{\ln(2A)} \int_{-1/2}^{1/2} [\boldsymbol{v}_D - Pe^E \boldsymbol{v}_S] \cdot \boldsymbol{p}_j s_j \mathrm{d}s_{j,} \tag{3.9}$$

which represents a set of N equations, one for each particle, coupled to all other particle stresslets through the disturbance velocity term.

When the point of closest approach between two particles comes within a specified multiple of the particle radius, near-field lubrication forces become important and must be included in the expression of the total force. Because near-field hydrodynamic effects are excluded as a result of the slender-body approximation, lubrication forces are simply additive and the far-field hydrodynamic expressions need not be modified. The force acting on two particles in close contact is dependent on their relative orientations and velocities $\dot{h}$, as well as their distance of closest approach h. Originally derived in Claeys & Brady (1989), we refer the readers to Butler & Shaqfeh (2002), where the equations for the lubrication force for each interaction type are reproduced.

Because the lubrication forces are dependent on the each particle's relative velocity, the lubrication forces couple the equations of motion (3.1) and (3.2) with the stresslet equations. The relative motions $\dot{h}$ must therefore be solved simultaneously with the stresslet equations for those particles experiencing lubrication interactions. For this reason, lubrication interactions significantly increase the computational overhead of the simulations because the size of the stresslet system that must be solved iteratively also increases.

3.2.2. *Smooth particle mesh Ewald (SPME) algorithm*

The stresslet equations (3.9) may be solved directly (i.e. by matrix inversion) if traditional Ewald sums are used because the stresslets appear explicitly in the disturbance velocity. Ewald sums, however, are computationally expensive to compute and severely limit the size of the system that may be studied. To overcome this issue, we use an algorithm developed by Saintillan *et al.* (2005) for simulation of rigid fibres : a smooth particle mesh Ewald algorithm. Motivated by that of Essman *et al.* (1995), the algorithm makes use of the $n \ln n$ scaling of the fast Fourier transform (FFT) to significantly reduce the cost of computing hydrodynamic disturbances. In this algorithm, the disturbance velocities at each quadrature point for each fibre are computed by interpolating the complex exponentials appearing in the Ewald formulation of equation (3.4) onto a fixed grid and using the FFT to compute all velocities simultaneously. The particle forces (and therefore stresslets) do not appear explicitly; this demands an iterative solution for (3.9).

We omit the algorithmic details in this paper and refer the reader to Saintillan's work for further information.

3.3. *Brownian motion*

For simplicity of notation, we adopt the convention of Butler & Shaqfeh (2005) and write (3.1) and (3.2) for all particles in a compact mobility formulation as

$$\left\{ \begin{array}{c} \dot{\boldsymbol{x}} \\ \dot{\boldsymbol{p}} \end{array} \right\} = \boldsymbol{U}_S + \mathscr{M} \cdot \left\{ \begin{array}{c} \mathscr{F}^0 \\ \mathscr{F}^1 \end{array} \right\}, \tag{3.10}$$

where the superscript m on $\mathscr{F}$ represents the mth moment of the force distribution $\mathscr{F}^m = \int \boldsymbol{f}(s) s^m ds$ and $\boldsymbol{U}_S$ is a vector describing the net particle motion due to the surface slip velocity. From (3.1) and (3.2), it can be seen that

$$\boldsymbol{U}_S = \left\{ \begin{array}{c} 0 \\ -12Pe^E(\boldsymbol{I} - \boldsymbol{pp}) \cdot \displaystyle\int_{-1/2}^{1/2} \boldsymbol{v}_S(s) s \, \mathrm{d}s \end{array} \right\}.$$

Each vector in (3.10) represents the concatenation of the forces or velocities of all particles and has therefore $3N$ (bracketed terms) or $6N$ (non-bracketed terms) components. $\mathscr{F}^0$ is simply the total force vector $\mathscr{F}$ while $\mathscr{F}^1$ is related to the torque via

$$\mathscr{T} = \boldsymbol{p} \wedge \mathscr{F}^1 \qquad \mathscr{T} \wedge \boldsymbol{p} = (\boldsymbol{I} - \mathbf{pp}) \cdot \mathscr{F}^1. \tag{3.11}$$

$\mathscr{M}$ is the grand mobility tensor ($6N \times 6N$ components), which is only a function of the suspension geometry and implicitly incorporates the stresslet contribution to the force density as written in (3.8). The mobility formulation (3.10) allows for convenient specification of the Brownian force via its first two moments as

$$\left\langle \left\{ \begin{array}{c} \mathscr{F}^0_B \\ \mathscr{F}^1_B \end{array} \right\} \right\rangle = \mathbf{0}$$

as well as

$$\left\langle \left\{ \begin{array}{c} \mathscr{F}^0_B \\ \mathscr{F}^1_B \end{array} \right\} \otimes \left\{ \mathscr{F}^0 \mathscr{F}^1 \right\} \right\rangle = 2\delta(t - t') \mathscr{M}^{-1},$$

which satisfies the fluctuation dissipation theorem. In our numerical simulations, we discretely model the fluctuating Brownian force between time t and $t + \Delta t$ using a $6N$ vector $\mathscr{W}$ with each component independently normally distributed with mean 0 and unit variance:

$$\begin{Bmatrix} \mathscr{F}^0_B \\ \mathscr{F}_{\mathscr{B}}{}^1 \end{Bmatrix} = \sqrt{\frac{2}{\Delta t}} \mathscr{B} \cdot \mathscr{W}, \tag{3.12}$$

where $\mathscr{B}$ satisfies $\mathscr{M}^{-1} = \mathscr{B}\mathscr{B}^T$. Theoretically, one could evaluate the inverse of the mobility and determine $\mathscr{B} = \mathscr{M}^{-1/2}$ (non-uniquely) via Cholesky decomposition or diagonalization to obtain the Brownian force. However, when using the SPME algorithm, one cannot separate the grand mobility tensor from the net force because the velocity disturbances $\boldsymbol{v}_D$ on each fibre are evaluated simultaneously. Rather, we use an iterative method developed by Fixman (1986) in which we write the Brownian force as a Chebychev polynomial expansion in the mobility. Computation details are provided in Santillan *et al.* (2006*d*).

It should be noted that due to the constraint that each vector $\boldsymbol{p}$ must retain unit length, the grand mobility tensor $\mathscr{M}$ must first be first factored (Butler & Shaqfeh 2005) as $\mathscr{M} = \mathscr{K} \cdot \widetilde{M} \cdot \mathscr{K}$, where

$$\mathscr{K} = \begin{bmatrix} \boldsymbol{I} & 0 \\ 0 & \boldsymbol{I} - \boldsymbol{pp} \end{bmatrix}.$$

The factorization is evident when (3.11) is substituted in (3.2). In our implementation, Fixman's algorithm is applied to $\widetilde{M}$ followed by the application of the constraint matrix $\mathscr{K}$.

3.4. *Integration*

Once the Brownian forces are computed as discussed in § 3.3, the net force is compiled and the total particle velocities and stresslets are determined. Although high-order integration schemes may be used, we employ a simple Euler stepping to calculate the net displacement between time steps. We rationalize this choice by calling attention to the Brownian force term that appears as a realization of a random variable with standard deviation of $\mathscr{O}(\Delta t^{-1/2})$. Upon integration, the net displacements $\{\Delta \boldsymbol{x}, \Delta \boldsymbol{p}\}$ are only determinable to within $\mathscr{O}(\Delta t^{1/2})$. Thus, extra computational effort required to enhance integration accuracy for the deterministic components of the velocity equations is wasted.

We choose a fixed time step Δt based on the desired resolution of time scales within the simulation. To prevent collisions (particle overlap), this 'global' time step is separated into n 'local' time steps of non-uniform size δt_i, where $\Delta t = \sum_{i=0}^{n} \delta t_i$. For each local time step, the calculated Brownian force and far-field hydrodynamic interactions remain constant, while the near-field lubrications and particle displacements are updated based on the current configuration. The magnitude δt_i is chosen after each local time step by determining the minimum estimated time for fibre collision within the suspension. Butler & Shaqfeh (2002) found that this local lubrication update approximation greatly enhanced simulation speed but did not affect overall dynamics given a sufficiently small Δt.

Our Euler stepping algorithm is simply given by

$$\begin{Bmatrix} \boldsymbol{x} \\ \boldsymbol{p} \end{Bmatrix} (t + \delta t) = \begin{Bmatrix} \boldsymbol{x} \\ \boldsymbol{p} \end{Bmatrix} (t) + \left[U_S + \mathscr{M} \cdot \begin{Bmatrix} \mathscr{F}^0 \\ \mathscr{F}^1 \end{Bmatrix} + \nabla \cdot \mathscr{M} \right] \delta t, \tag{3.13}$$

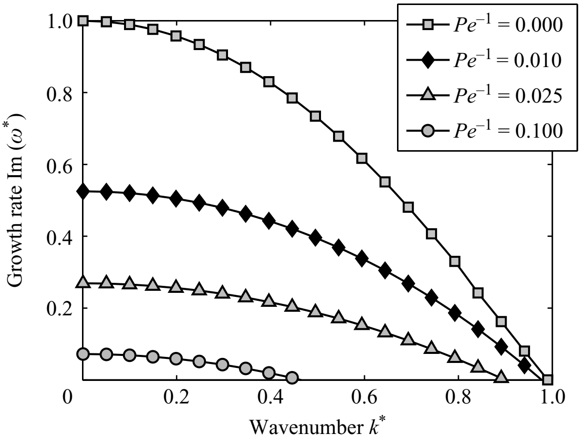

FIGURE 2. Instability growth rate ω vs. wavenumber k for various inverse Péclet numbers, for $nl_c^3 = 0.1$ and $A = 20$, solved for using the spectral expansion method described in § 2.2. The effect of Brownian motion is to suppress both the growth rate of the instability and to reduce the range of wave-numbers for which the suspension is unstable.

where the drift term is explicitly added because it is not implicitly captured in lower-order integration schemes (Banchio & Brady 2003). At time t, we estimate the drift velocity $\nabla \cdot \mathscr{M}$ as is done by Banchio & Brady (2003) by first calculating the Brownian velocity $U_B(t)$ as

$$U_B(t) = \mathscr{M} \cdot \begin{Bmatrix} \mathscr{F}_B^0 \\ \mathscr{F}_B^1 \end{Bmatrix},$$

where the Brownian force and torque are computed as described in the previous section. We then temporarily update the particle locations using only the Brownian velocity via

$$\begin{Bmatrix} \boldsymbol{x} \\ \boldsymbol{p} \end{Bmatrix} (t + \delta t_1) = \begin{Bmatrix} \boldsymbol{x} \\ \boldsymbol{p} \end{Bmatrix} (t) + U_B(t)\delta t_1$$

and re-evaluate the Brownian velocity $U_B(t + \delta t)$ using the updated positions for the evaluation of the mobility but the same Brownian forces. It is a simple exercise to show that $\overline{\nabla \cdot \mathscr{M}} = \Delta t / 2\delta t_1 (U_B(t + \delta t_1) - U_B(t)) + \mathscr{O}(\Delta t)$, and this approximate realization of the drift velocity remains constant throughout the global time step Δt.

4. Results and discussion

4.1. *Effects of Brownian motion*

We first utilize the spectral solution method for the mean field stability analysis to analyse the Brownian (no ICEP) problem described in § 2.1. Figure 2 shows the instability growth rate $\mathrm{Im}(\omega^*)$ as a function of scaled wavenumber $k^* = k/\sqrt{2\beta}$ and growth rate $\omega^* = \omega\sqrt{30/\beta}$. The scaling was chosen such that $\lim_{k\to 0} \mathrm{Im}(\omega^*) = 1$ and $\mathrm{Im}(\omega^*) = 1$ for $k^* = 1$ and $Pe^{-1} = 0$. It can be seen that as the Péclet number is decreased (corresponding to strong Brownian motion relative to settling velocity), the growth rate of the instability is suppressed and the wavenumber at which the instability disappears becomes smaller. The origin of both qualitative features is clearly visible from the first correction in the perturbation solution to the stability eigenvalue problem (2.20). Specifically, centre of mass diffusion tends to smooth

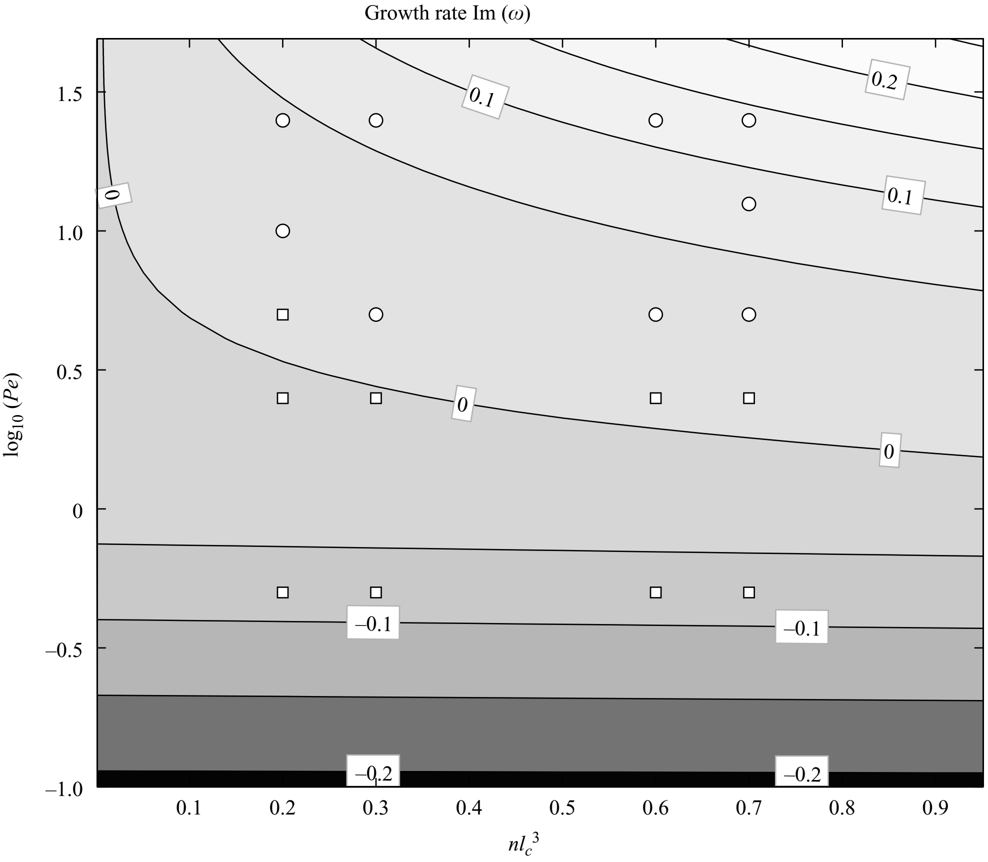

FIGURE 3. A stability phase contour plot of dimensionless number density vs. gravitational Péclet number for $A = 20$ and $k = 0.2513$. The contour colours (greyscale) represent the instability growth rate Im(ω). The zero contour represents a neutrally stable suspension. The white open circles correspond to unstable suspensions determined from Brownian dynamics simulations using the same parameters. The white squares correspond to stable simulated suspensions.

out short wavelength (large wavenumber) fluctuations because particles can quickly diffuse out of regions of higher concentration relative to the time scale of instability formation. This effect can clearly be seen in figure 2: as the Péclet number decreases, the wavenumber corresponding to a neutrally stable suspension $\omega = 0$ decreases. More important in the suppression of the instability is rotational diffusion, which randomizes particle orientations and counteracts the hydrodynamic torque applied through the buoyancy-driven instability mechanism. The primary effect of rotational diffusion is to dampen the growth rate of the instability for a fixed k. As $Pe \rightarrow 0$ the instability curve shrinks asymptotically to the origin; however, due to the singular limit at $k = 0$ one can always find a wavenumber at fixed Péclet number for which the instability growth rate is positive. Physically this limit corresponds to an unbounded suspension container but is of little physical consequence.

Figure 3 is a contour plot of the instability growth rate Im(ω) as a function of both the gravitational Péclet number and number concentration of particles for particles with $A = 20$. A logarithmic scale has been used to magnify the region of stable suspensions; however, it should be noted that the region of Brownian stabilization occurs in a relatively small region $0 < Pe \lesssim 2$. Marked on the figure are sample points from the Brownian dynamics simulations described in § 3, with squares representing stable suspensions and circles representing unstable ones (within the simulation time). To evaluate whether the instability will occur, we have used the criterion that the τ time moving average of the mean sedimentation velocity scaled by the maximum single particle settling velocity, $\mathrm{MA}(t, \langle U_z \rangle / U_M, \tau)$, exceeds and remains above 1.0 over the course of the simulation. We have chosen this interpretation of stability from our simulations for consistency with previous literature (Butler & Shaqfeh 2002; Saintillan *et al.* 2006*b*) and because the sedimentation velocity provides a reliable indicator for both essential features of the instability: formation of density perturbations and the growth of these perturbations over time. The moving average is simply defined as

$$\mathrm{MA}\,(t, x, \tau) = \frac{1}{\tau} \sum_i x(t + \delta t_i),$$

where $\sum_i \delta t_i = \tau$. The simulation maximum time is chosen based on the sedimentation time t_s, the time scale over which the instability develops from an isotropic suspension in the absence of Brownian motion, and is usually set at 120 t_s. Based on the non-dimensionalization scheme employed in the Brownian dynamics simulation, we have chosen $\tau = t_s/t_c = \pi/2Pe \ln(2A)$ to compute the moving average. The moving average exceeding 1.0 is indicative of cluster formation (and thus instability) because hydrodynamic interactions within clusters screen internal particles from viscous drag, allowing the cluster to achieve a higher settling velocity than an isolated fibre aligned with gravity in Stokes flow. We find that for fixed system sizes within our computational limitations (approximately 500 Brownian particles or several thousand non-Brownian), the fluctuations in average sedimentation velocity grow large for small Péclet numbers, and a moving average is necessary to smooth the fluctuations and isolate the underlying trend associated with cluster and streamer formation. This can be seen by considering the variance of the component of the Brownian velocity in the direction parallel to gravity, $\langle U_{Bz} U_{Bz} \rangle / U_M^2 \sim Pe^{-2} \Delta t^{-1}$; for a fixed time step the fluctuations decay as Pe^{-2}, so the moving average window decreases with increasing Péclet number.

We find that in general, the mean field theory predicts the onset of instability quite well. It should be noted, however, that prediction of instability very close to the neutral suspension curve $\omega = 0$ and for small nl_c^3 is very difficult, as it may require more simulation time than is feasible. Additionally, neglecting near-field interactions, as well as stress coupling in the hydrodynamic interactions within the mean field approximation may result in slight differences in both the Péclet number and concentration at which an instability occurs. The trend, however, is correct: as we move from left to right on the phase contour plot (increasing number concentration), crossing the neutral stability line at a constant Péclet number, the suspension becomes unstable. This occurs because the rotational velocity induced by the instability formation, increases with number concentration as a result of the increased magnitude of the density fluctuations.

In figure 4, we show the Brownian dynamics trajectories of two suspensions, both at $Pe = 10$ and $nl_c^3 = 0.2$, but with varying wavenumber. Examining the averaged orientation trajectories relative to the direction of gravity (right panel), we see that for both values of k, suspensions are very nearly isotropically oriented for the majority of the simulation, indicating strong rotational diffusion. For the suspension for $k = 0.2513$, however, the mean orientation departs significantly from isotropic by

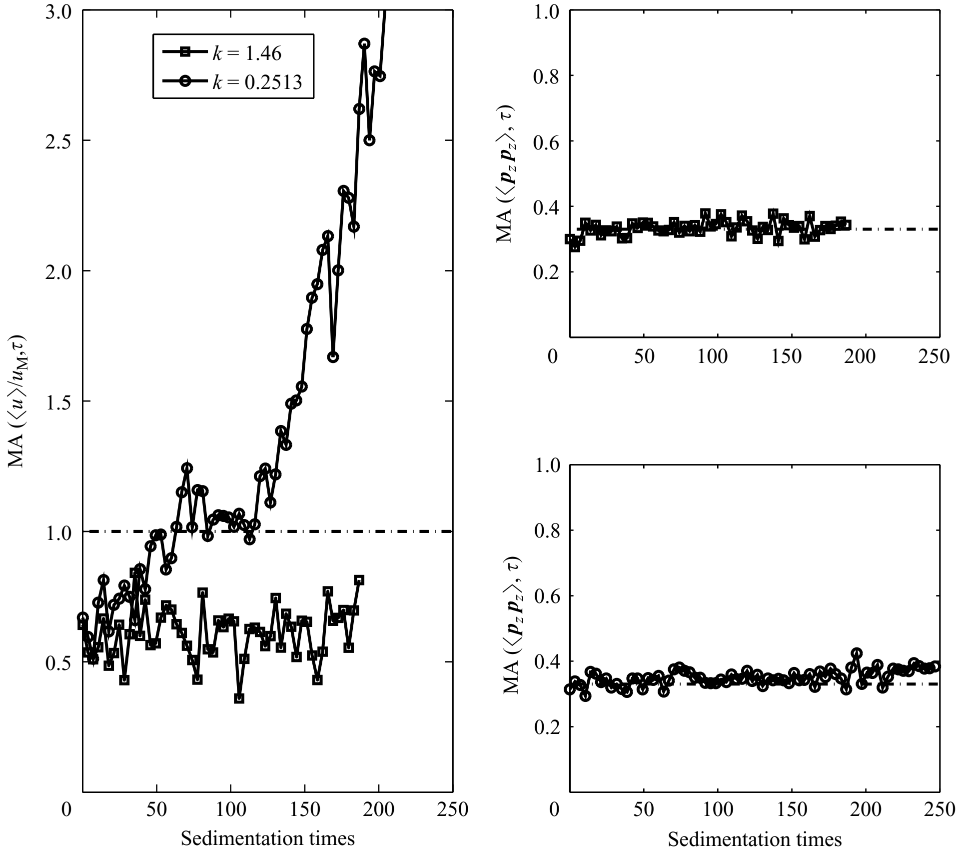

FIGURE 4. Brownian dynamics trajectories of a suspension with $Pe = 10$, $A = 20$ and $nl_c^3 = 0.2$, varying the minimum allowable k from 0.2513 to 1.46. The suspension is stable for large wavenumber (smaller boxes) but becomes unstable as k is decreased. Left panel: the moving average (MA) of the sedimentation velocities. Right panel: the MA of the second moment of $\boldsymbol{p}$ in the direction of gravity.

$t = 250$. As k is decreased from 1.46 to 0.2513 by changing the simulation box size, the suspension clearly becomes unstable. Although the average sedimentation velocity diverges from 1.0 in the unstable suspension, centre of mass diffusion acts to prevent rapid densification of streamers. Because the instability is hydrodynamic in nature and therefore long-ranged, we observe the divergence of the sedimentation velocity with increasing Péclet number more quickly than increased orientation with gravity, the latter of which is magnified by excluded volume and lubrication interactions within dense clusters. This result agrees with the predictions of the mean field analysis as presented in figures 2 and 3, which predict a decreasing growth rate with increasing wavenumber at constant Péclet.

Figure 5 shows images of the simulated structure of two suspensions at a number concentration of $nl_c^3 = 0.6$ and particles of $A = 20$, after 60 sedimentation times t_s/t_c. Clearly, the suspension in the top panel maintains a nearly isotropic structure in both orientation and centre of mass while the bottom suspension develops a single dense streamer surrounded by a clarified fluid, oriented preferentially in the direction of gravity. Generally, simulations of the unstable suspensions produce a single dense

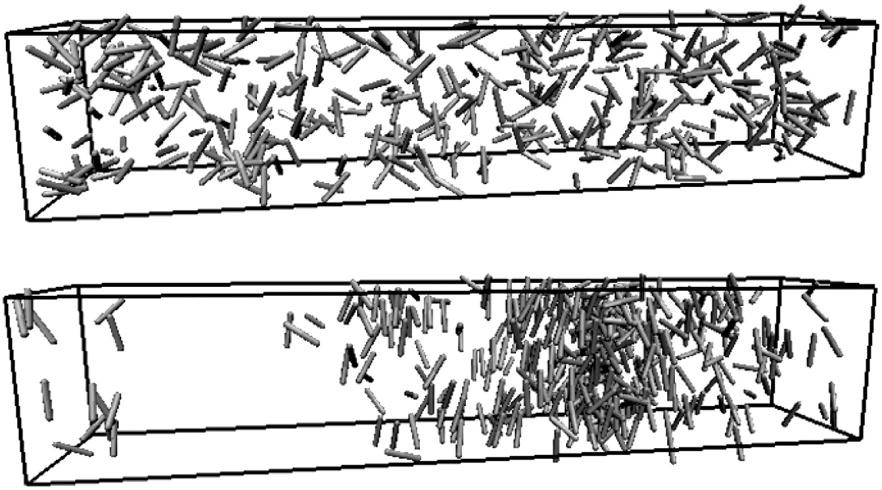

FIGURE 5. Image of a stable and unstable Brownian suspension in a box of aspect ratio 25:5:5, $nl_c^3 = 0.6$, $A = 20$ after 60 sedimentation times t_s/t_c. Top panel: $Pe = 0.5$ ($\log_{10}(Pe) = -0.3$), corresponding to the 'stable' region on the above phase plot. Bottom panel: $Pe = 25$ ($\log_{10}(Pe) = -1.40$), corresponding to the 'unstable' region. A streamer clearly forms in the unstable suspension and the moving average of the mean sedimentation velocity $\mathrm{MA}(t, \langle U_z \rangle / U_M, \tau)$ exceeds 1.0 (see below).

streamer as opposed to multiple streamers because the largest wavelength disturbance has the highest growth rate. In a non-periodic system, however, density stratification or wall effects can contribute to a wavenumber selection as was observed in point particle simulations by Saintllian *et al.* (2006*a*).

In figure 6 we present the trajectories associated with figures 3 and 5. The two left panels show the moving average of the mean sedimentation velocity for various Péclet numbers, while the right panels show the mean orientation of the fibres relative to the direction of gravity. As is predicted by the mean field theory, the suspension with the largest Péclet number, $Pe = 25$, (weakest Brownian motion) is the most unstable and therefore has the highest growth rate, with the mean normalized sedimentation velocity diverging quickly and irreversibly from 1.0. In this case, the mean orientation $\langle p_z p_z \rangle$ quickly departs from the orientationally isotropic value of 1/3 due to densification and cluster formation.

As the Péclet number is reduced, corresponding to increased dominance of thermal motion, the instability forms more slowly, as demonstrated by the suspension with $Pe = 5$ (top panel). In this case, the mean velocity diverges more slowly, and the orientation remains nearly isotropic. We conclude that although the $Pe = 5$ case is unstable, it is only marginally so, because the instability mechanism is nearly counterbalanced by rotational diffusion as evidenced by the orientation plot (and as explained above, the orientation is a lagging indicator). As the Péclet number is subsequently reduced to 2.5 and 0.5, we observe stabilization of the suspension characterized by isotropic orientation distributions and mean velocities that do not remain above 1.0 for a significant amount of simulation time. Excursions of the velocity above 1.0 in both cases are simply due to Brownian fluctuations and cannot be completely eliminated. Increasing the moving average window size reduces this effect, but requires significantly more computer time.

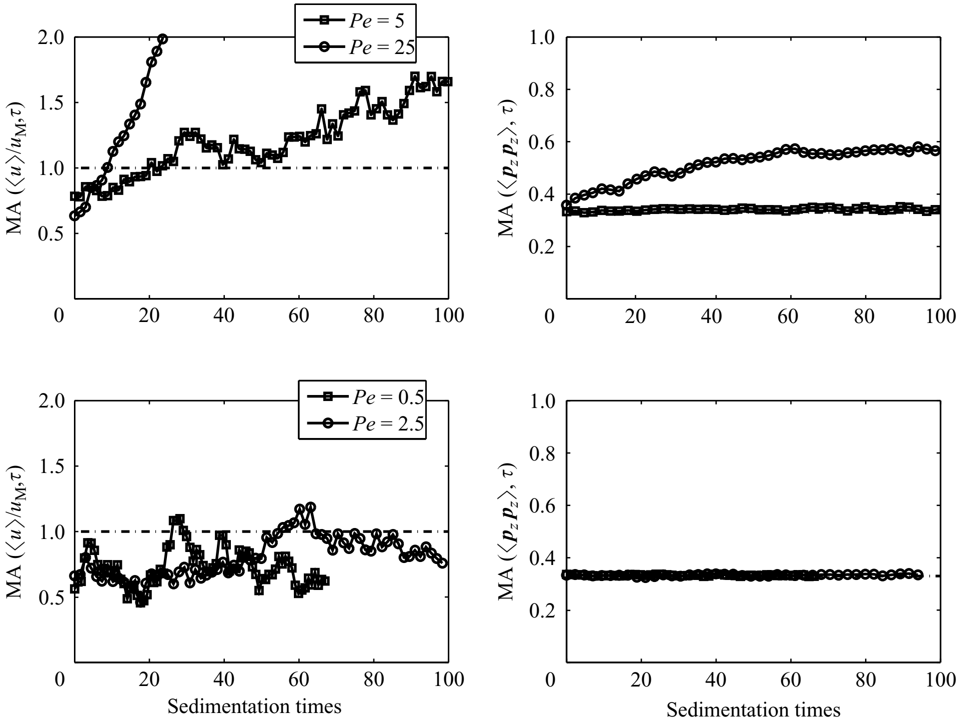

FIGURE 6. Left panels: Trajectories of the mean suspension sedimentation velocityU_z scaled by the maximum velocity of an isolated particle for a suspension of particles with $A = 20$, $nl_c^3 = 0.6$, and $k = 0.2513$ for Péclet numbers of 0.5, 2.5, 5, and 25 ($\log_{10}(Pe) = -0.3, 0.4, 0.7, 1.4$). When the instability develops for sufficiently large Péclet number, dense clusters and streamers form within the suspension and cause the average scaled sedimentation velocity to exceed 1.0. Right panels: The average orientation with respect to the direction of gravity. Lubrication and excluded volume interactions within the streamer tend to rapidly align particles with gravity. This effect is only observed for the $Pe = 25$ case.

4.2. *Brownian motion and ICEP*

In §4.1, we considered solely the effect of Brownian motion on the sedimentation instability. We now consider the net effect of Brownian motion, sedimentation and induced charge electrokinetic phenomenon on the instability, which constitutes a rich interplay of physical phenomena. Saintillan *et al.* (2006*b*) addressed stabilization of a suspension of non-Brownian particles through ICEP and concluded that the rotational velocity due to the instability mechanism (i.e. concentration perturbations) could be effectively cancelled by rotation due to the surface slip induced by ICEP in a sufficiently strong electric field. In their work, they present a stability phase diagram as a function of H and nl_c^3 at a fixed k. They find that the critical value of H to achieve stabilization grows as $(nl_c^3)^{0.54}$ because the angular velocities induced by concentration fluctuations approximately balance those of ICEP with this scaling.

In contrast, Brownian suspensions subjected to an electric field do not deterministically align with the electric field; rather, the alignment in the suspension is characterized by a balance between Brownian torques and electrokinetic rotation through a probability density function ((2.4) above). Therefore, in sedimenting Brownian suspensions in electric fields, thermal motion will change the orientation distribution to state that is less stable to concentration fluctuations than a more

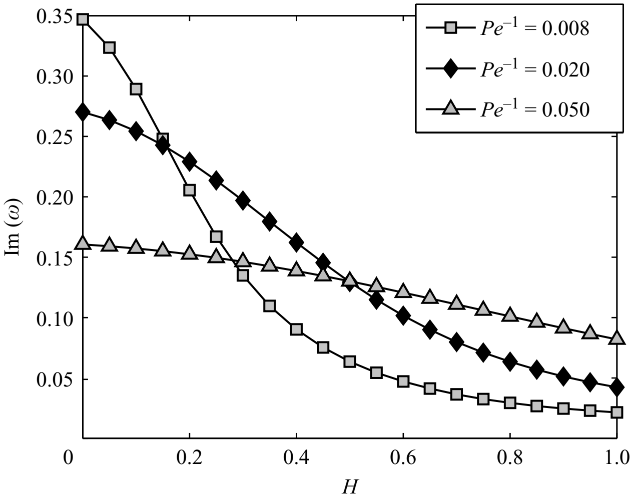

FIGURE 7. Instability growth rate vs. dimensionless electric field strength (H) for several inverse Péclet numbers for a suspension with $A = 20$, $k = 10^{-3}$ and $nl_c^3 = 1.0$. For small H, the most unstable suspensions occur for small inverse Péclet (weak Brownian motion). There is a behavioural inversion for large H and intermediate inverse Péclet numbers, where thermal motion disrupts the stabilizing effect of alignment.

aligned state; this occurs when the Brownian torque partially offsets the alignment effects of ICEP. Recalling the conclusions from the previous section, this suggests that there exists a parameter set for which, at a fixed electric field strength relative to gravity, Brownian motion will destabilize the suspension through randomization of the otherwise stabilizing alignment.

We expect the effects of the electric field to be approximately cancelled when $|\dot{\boldsymbol{p}}_B| \sim |\dot{\boldsymbol{p}}_{ICEP}|$, where $|\dot{\boldsymbol{p}}_B|$ is the magnitude of the rotation induced by Brownian motion. From (3.2), this occurs approximately when $Pe^E \sim 3\ln(2A)/\pi$, or about 3 for a particle with aspect ratio 20. The suspension will only be destabilized via thermal motion if it would otherwise be unstable with no electric field present. This condition is summarized by figure 3.

We present in figure 7 the results of the mean field stability analysis in which we vary the strength of the electric field relative to gravity (represented by the parameter H defined in 2.13) at a fixed wavenumber, number concentration, and gravitational Péclet number. The trend for all values of Péclet number examined is that increasing electric field strength lowers the instability growth rate, stabilizing the suspension. This result is consistent with observations by Saintillan *et al.* and can also be seen in figure 8, where we present the effect of increasing field strength for a constant Péclet number and varying wavenumber. Note, however (in figure 7), that at low field strengths, the suspensions corresponding to the weakest Brownian motion are the least stable (low Pe^{-1}), while for high field strengths ($H \gtrsim 0.3$) the suspensions corresponding to strongest Brownian motion are the least stable. This behavioural inversion agrees with our predictions of a region of Brownian-induced destabilization.

Figure 9 shows the instability growth rate as a function of wavenumber for fixed $H = 1.0$ and Péclet number. As the Péclet number decreases (going from curves 1–4), the thermal motion first decreases the instability growth rate (curves 1–2, $Pe^E \sim 117/23$) primarily as a result of centre of mass Brownian motion; next, the instability growth rate increases (curves 2–3 $Pe^E \sim 23/3.9$) as a result of the thermal

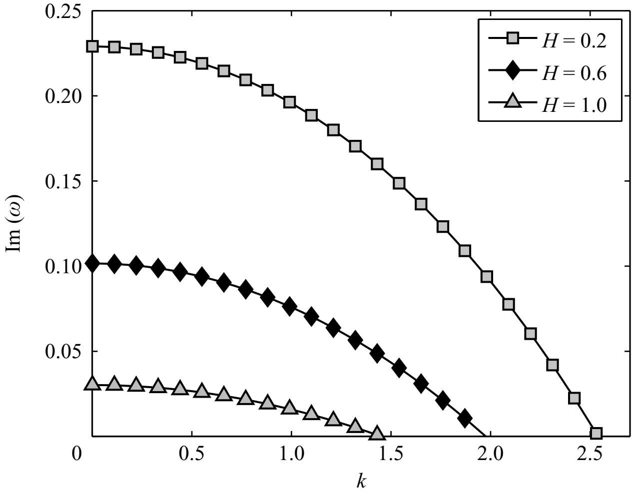

FIGURE 8. Instability growth rate vs. wavenumber for various electric field strengths for a fixed Péclet number of 50. $A = 20$, and $nl_c^3 = 1.0$. The suspensions are consistently most unstable for small wavenumber. Stabilization occurs as H is increased.

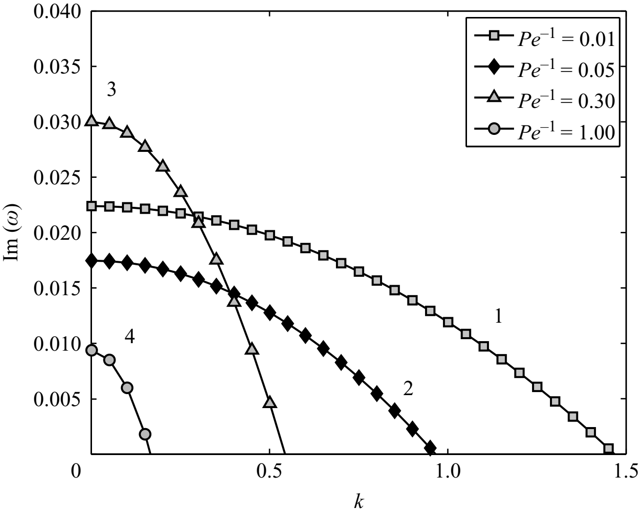

FIGURE 9. Instability growth rate vs. wavenumber for various inverse Péclet numbers at a constant $H = 1.0$ and $nl_c^3 = 1$. A maximum growth rate occurs for small wavenumbers and intermediate Péclet numbers as Brownian motion offsets the 'stability gains' achieved through ICEP stabilization. At higher Péclet numbers the Brownian motion becomes the dominant stabilization mechanism and the growth rate declines.

destabilization mechanism. Finally, the growth rate continues to decrease as thermal motion becomes dominant (curves 3–4 $Pe^E \sim 3.9/1.2$). The electric Péclet numbers presented are in a reasonable agreement with our scaling argument presented above (i.e. $Pe^E \sim 3$ for destabilization). We note that centre of mass diffusion always acts to stabilize suspensions because it uniformly disperses regions of high concentration without interfering with the stabilizing effects of the electric field.

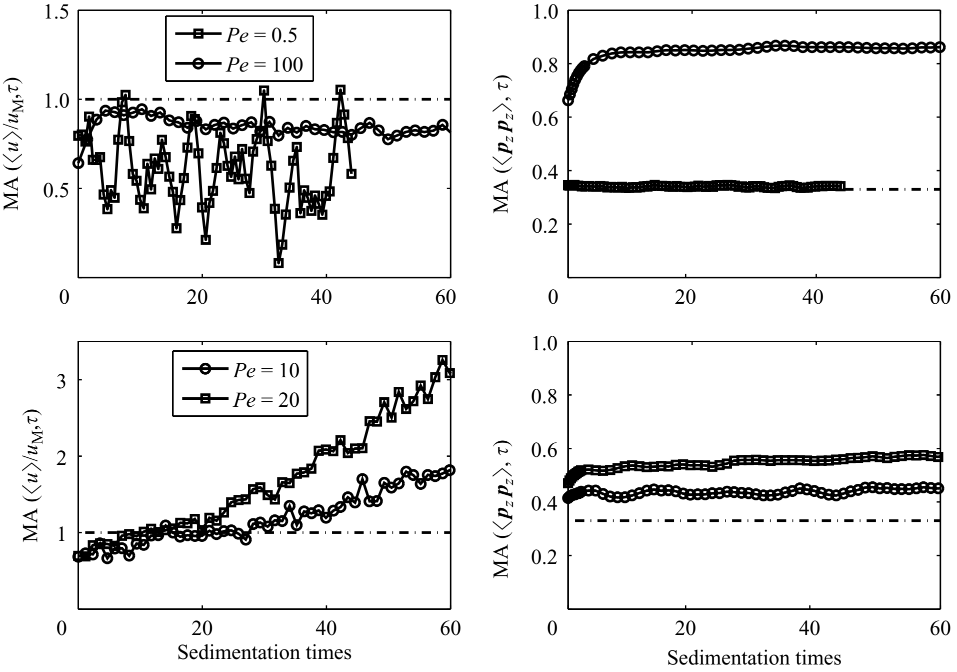

FIGURE 10. Left panels: Trajectories of the mean suspension sedimentation velocityU_z scaled by the maximum velocity of an isolated particle for a suspension of particles with $A = 20$, $nl_c^3 = 0.6$, $k = 0.2513$ and $H = 0.6$ for gravitational Péclet numbers of 0.5, 10, 20 and 100 ($\log_{10}(Pe) = -0.3, 1.0, 1.3, 2.0$). The electric field stabilizes the suspension in the case of weak Brownian motion ($Pe = 100$, top) by resisting the rotation induced by concentration fluctuations. As thermal motion becomes more important, the electric stabilization effect is minimized and the instability occurs ($Pe = 10/20$, bottom). As the Péclet number is reduced further, Brownian motion dominates and the suspension is stabilized in an isotropic orientation (top). Right panels: The average orientation with respect to the direction of gravity. For weak Brownian motion the particles are very aligned and reduce towards isotropic orientation as the Péclet number is lowered. In this case, suspensions characterized by extremes in alignment (very high and isotropic) are stable (top panels).

The results of our scaling argument and mean field analysis are strengthened by identical observations from our Brownian dynamics simulations. In figure 10 we present average sedimentation velocities and orientation in a suspension with $A = 20$, $nl_c^3 = 0.6$, $k = 0.2513$ and fixed $H = 0.6$ for gravitational Péclet numbers of 0.5, 10, 20 and 100. Clearly, for high Péclet numbers (weak Brownian motion) the electric field strongly aligns the suspension, resisting hydrodynamic torques that cause the instability to form. This is shown in the top-right panel where the average orientation in the direction of gravity approaches 0.85. The average sedimentation velocity within the suspension never exceeds 1.0, indicating an absence of clusters that characterize an unstable suspension. As the Péclet number is reduced (strengthening thermal motion), the effect of electrokinetic alignment is mitigated and the average scaled sedimentation velocity clearly exceeds 1.0, with $\mathrm{Im}(\omega)(Pe = 10) < \mathrm{Im}(\omega)(Pe = 20)$. The instability growth rate therefore must pass through a maximum between $Pe = 100$ and $Pe = 20$, which correspond to $Pe^E = 70$ and $Pe^E = 14$ (cf. (3.3)). At substantially lower gravitational Péclet numbers, the strength of Brownian motion dominates and again stabilizes the suspension. We present in figure 11 simulation images after 60

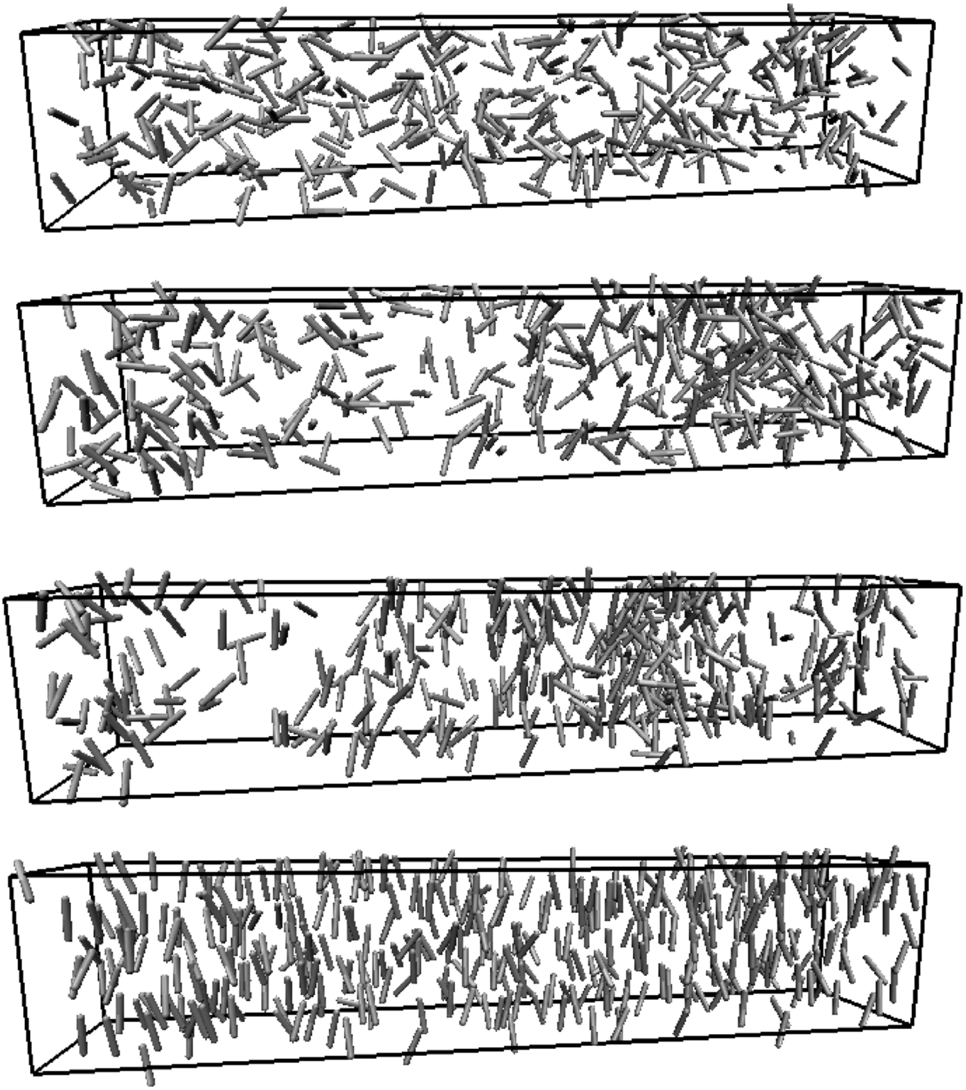

FIGURE 11. Snapshots of suspension structure for $A = 20$, $nl_c^3 = 0.6$, $k = 0.2513$ and $H = 0.6$ at gravitational Péclet numbers of 0.5 (top), 10 (mid-top), 20 (mid-bottom) and 100 (bottom). The top and bottom images show suspensions stabilized in an isotropic and aligned state, respectively, while the middle images show clustering characteristic of an unstable suspension.

sedimentation times of suspensions with a fixed $H = 0.6$ and varying Péclet number. The top and bottom images show suspensions stabilized in an orientationally isotropic and aligned state, respectively, while the middle images show clustering characteristic of an unstable suspension. These observations are clearly in agreement with our stability analysis results and simulated sedimentation trajectories.

Our results demonstrate that the phase plot presented in Saintillan *et al.* (2006*b*) is an incomplete description of the phase space characterizing the instability. Foremost, Saintillan *et al.* present results in the limit of no thermal motion ($Pe \rightarrow \infty$) which therefore do not capture the initially destabilizing effects of Brownian motion. Second, we have shown through our mean-field theory and Brownian dynamics simulations that at fixed electric field strength and Péclet number, the onset of the instability is wavenumber dependent, occurring only for sufficiently large box sizes. For a complete description of the concentration instability, thermal motion, box size, and number density must all be considered.

A thermally induced instability is perhaps somewhat counter-intuitive. In general, one might expect Brownian motion to counteract the destabilizing effects of gravitational settling, leading to a stable suspension. We have, however, identified a system in which thermal motion can act to destabilize suspensions by counteracting the effects of an otherwise stabilizing field. This phenomenon of Brownian-induced demixing may occur for a variety of other physical systems, and may be observed when the stability of a system is determined by the response of a microstructural variable (i.e. particle alignment, particle separation distance, etc.) to an external field or interparticle potential. A similar analysis to the one performed here may thus be applied to such systems as particle stabilized emulsions or electrostatically stabilized sols, for example.

In summary, we have shown via Brownian dynamics and mean field theory that Brownian motion plays a crucial role in determining the stability of sedimenting suspensions of anisotropic particles. Depending on the collective effect of many fundamentally different physical interactions, Brownian motion can either act to stabilize or destabilize sedimenting suspensions. In suspensions with no external torques, Brownian motion stabilizes the mean sedimentation velocity by randomizing the particle orientation towards an isotropic state, resisting any collective hydrodynamic effects that lead to instability. If external torques are applied (hydrodynamically via ICEP or otherwise) that tend to align the particles and provide an alternate stabilization mechanism, the randomization caused by Brownian motion may have a destabilizing effect. This is of critical importance when designing devices that utilize the collective physical phenomena to achieve function. For instance, in the design of a ‘nano-barcode’ reader, both stability and alignment (for detection purposes) must be assured, so one should operate in a regime of electric field strengths which counteract both the instability mechanism created through concentration fluctuations as well as destabilization by orientational randomization due to thermal motion.

The authors would like to acknowledge the contribution of David Saintillan, who laid much of the foundation for this work. We would also like to thank the Army High Performance Computing Research Center (AHPCRC) at Stanford as well as the National Science Foundation under Grant CBET-0729771 for funding.

Appendix. Spectral solution details

Beginning with (2.12), we make the substitution $\tilde{c} = \sum_{q=0}^{q=\infty} \sum_{s=-q}^{s=q} a_{qs} Y_q^s$, giving

$$
\begin{aligned}
0 = {} & -\mathrm{i}\omega \sum_{qs} a_{qs} Y_q^s + \frac{2\sqrt{\pi}\mathrm{i}\beta\Psi}{k^2} (\boldsymbol{p}\cdot\hat{\boldsymbol{z}})(\boldsymbol{p}\cdot\boldsymbol{k}) a_{00} \\
& + \frac{1}{2} H G_{\parallel} G_{\perp} \left\{ \left[1 - 3(\boldsymbol{p}\cdot\boldsymbol{e}_{\infty})^2\right] \sum_{qs} a_{qs} Y_q^s + (\boldsymbol{p}\cdot\boldsymbol{e}_{\infty})\boldsymbol{e}_{\infty} \cdot \sum_{qs} a_{qs} \nabla_{\boldsymbol{p}} Y_q^s \right\} \\
& - \frac{2\sqrt{\pi}\mathrm{i}\beta h(\boldsymbol{p})}{3k^2} (\boldsymbol{p}\cdot\boldsymbol{k}) \left[(\boldsymbol{e}_{\infty}\cdot\hat{\boldsymbol{z}}) - (\boldsymbol{p}\cdot\boldsymbol{e}_{\infty})(\boldsymbol{p}\cdot\hat{\boldsymbol{z}})\right] a_{00}
\end{aligned}
$$

$$
-\frac{\mathrm{i}}{2}(\boldsymbol{p}\cdot\boldsymbol{k})(\boldsymbol{p}\cdot\hat{\boldsymbol{z}})\sum_{qs} a_{qs}Y_q^s + 3Pe^{-1}\sum_{qs} a_{qs}q(q+1)Y_q^s
+\frac{1}{4}Pe^{-1}\left[k^2+(\boldsymbol{p}\cdot\boldsymbol{k})^2\right]\sum_{qs} a_{qs}Y_q^s, \qquad \text{(A 1)}
$$

where we have used the following properties of the spherical harmonics to simplify the expression:

$$
\int Y_q^s \mathrm{d}\boldsymbol{p} = 2\sqrt{\pi}\delta_{q0}\delta_{s0},
$$

$$
\nabla_{\boldsymbol{p}}^2 Y_q^s = q(q+1)Y_q^s.
$$

Noting that the spherical harmonics are orthonormal over the inner product space defined,

$$
\int Y_q^s Y_{q'}^{s'} \mathrm{d}\boldsymbol{p} = \delta_{qq'}\delta_{ss'}, \qquad \text{(A 2)}
$$

we then take the inner product of (A 1) with $Y_{q'}^{s'}$(and replacing $\boldsymbol{e}_\infty$ with $\hat{z}$ for electric fields aligned in the direction of gravity), giving

$$
\begin{aligned}
0 = {} & -\mathrm{i}\omega a_{q's'} + \frac{2\sqrt{\pi}\mathrm{i}\beta a_{00}}{k^2}\int \Psi(\boldsymbol{p}\cdot\hat{\boldsymbol{z}})(\boldsymbol{p}\cdot\boldsymbol{k})\bar{Y}_{q'}^{s'}\mathrm{d}\boldsymbol{p} \\
& +\frac{1}{2}HG_{\parallel}G_{\perp}\left\{\sum_{qs} a_{qs}\int\left[1-3(\boldsymbol{p}\cdot\hat{\boldsymbol{z}})^2\right]Y_q^s\bar{Y}_{q'}^{s'}\mathrm{d}\boldsymbol{p} + \sum_{qs} a_{qs}\int \bar{Y}_{q'}^{s'}(\boldsymbol{p}\cdot\hat{\boldsymbol{z}})\hat{\boldsymbol{z}}\cdot\nabla_{\boldsymbol{p}}Y_q^s\mathrm{d}\boldsymbol{p}\right\} \\
& -\frac{2\sqrt{\pi}\mathrm{i}\beta a_{00}}{3k^2}\int h(\boldsymbol{p})(\boldsymbol{p}\cdot\boldsymbol{k})\left[1-(\boldsymbol{p}\cdot\hat{\boldsymbol{z}})^2\right]\bar{Y}_{q'}^{s'}\mathrm{d}\boldsymbol{p} - \frac{\mathrm{i}}{2}\sum_{qs} a_{qs}\int(\boldsymbol{p}\cdot\boldsymbol{k})(\boldsymbol{p}\cdot\hat{\boldsymbol{z}})Y_q^s\bar{Y}_{q'}^{s'}\mathrm{d}\boldsymbol{p} \\
& +3Pe^{-1}q'(q'+1)a_{q's'} + \frac{1}{4}Pe^{-1}k^2a_{q's'} + \frac{1}{4}Pe^{-1}\sum_{qs} a_{qs}\int(\boldsymbol{p}\cdot\boldsymbol{k})^2Y_q^s\bar{Y}_{q'}^{s'}\mathrm{d}\mathbf{p}. \qquad \text{(A 3)}
\end{aligned}
$$

To proceed, we express the spherical harmonics in a more convenient form showing explicitly their dependence on the spherical coordinates $\theta \in [0, 2\pi]$ and $\phi \in [0, \pi]$.

$$
Y_q^s = N_{qs}L_q^s(\cos\phi)\mathrm{e}^{\mathrm{i}s\theta},
$$

where L_q^s are the associated Legendre polynomials of degree q and order s, and we take the vector $\boldsymbol{p}$ to be defined on the unit sphere as $\boldsymbol{p} = \{\cos\theta\sin\phi, \sin\theta\sin\phi, \cos\phi\}$. N_{qs} is a normalization constant given by

$$
N_{qs} = \sqrt{\frac{2(q+1)(q-s)!}{4\pi(q+s)!}}.
$$

Many of the integrands in (A 3) are simply products of the spherical harmonics with projections of $\boldsymbol{p}$; for instance, the 'dipole' term $\boldsymbol{p}\cdot\hat{\boldsymbol{z}}$ may be written in terms of the spherical coordinates as $\cos\phi$. Using this notation, we make use of several identities pertaining to the product of multipoles and the spherical harmonics. Those relevant to this discussion are listed in table 1. These identities reduce the multipolar integrands (through recursive application) to sums of spherical harmonics of differing degree. We may then use identity (A 2) to evaluate the remaining integrals; the results obtained are algebraic combinations of the coefficients A, B and C (see table 1), which avoids

Product	Result	Coefficients	
$\cos\phi Y_q^s$	$A_{qs}^1 Y_{q+1}^s + A_{qs}^2 Y_{q-1}^s$	$A_{qs}^1 = \left[\frac{(q-s+1)(q+s+1)}{(2q+1)(2q+3)}\right]^{1/2}$	$A_{qs}^2 = \left[\frac{(q-s)(q+s)}{(2q-1)(2q+1)}\right]^{1/2}$
$\mathrm{e}^{\mathrm{i}\theta}\sin\phi Y_q^s$	$B_{qs}^1 Y_{q+1}^{s+1} + B_{qs}^2 Y_{q-1}^{s+1}$	$B_{qs}^1 = -\left[\frac{(q+s+1)(q+s+2)}{(2q+1)(2q+3)}\right]^{1/2}$	$B_{qs}^2 = \left[\frac{(q-s)(q-s-1)}{(2q-1)(2q+1)}\right]^{1/2}$
$\mathrm{e}^{-\mathrm{i}\theta}\sin\phi Y_q^s$	$C_{qs}^1 Y_{q+1}^{s-1} + C_{qs}^2 Y_{q-1}^{s-1}$	$C_{qs}^1 = \left[\frac{(q-s+1)(q-s+2)}{(2q+1)(2q+3)}\right]^{1/2}$	$C_{qs}^2 = -\left[\frac{(q+s)(q+s-1)}{(2q-1)(2q+1)}\right]^{1/2}$

TABLE 1. Spherical harmonic identities used in reducing the multipolar integrands to simple products of harmonics.

numerical integration and greatly enhances solution speed. As an example, taking the wave-vector $\boldsymbol{k}=\{k, 0, 0\}$, the term $\int(\boldsymbol{p}\cdot\boldsymbol{k})^2 Y_q^s \bar{Y}_{q'}^{s'} d\,\boldsymbol{p}$ can be evaluated as:

$$
\begin{aligned}
\frac{1}{k^2}\int(\boldsymbol{p}\cdot\boldsymbol{k})^2 Y_q^s \bar{Y}_{q'}^{s'} d\,\boldsymbol{p} = {} & \frac{1}{4}\left[B_{qs}^1 B_{q+1,s+1}^1 \delta_{q',q+2}\delta_{s',s+2} + B_{qs}^1 B_{q+1,s+1}^2 \delta_{q'q}\delta_{s',s+2}\right. \\
& \left. + B_{qs}^2 B_{q-1,s+1}^1 \delta_{q'q}\delta_{s',s+2} + B_{qs}^2 B_{q-1,s+1}^2 \delta_{q-2,q'}\delta_{s',s+2}\right] + \frac{1}{2}\delta_{q'q}\delta_{s's} \\
& - \frac{1}{2}\left[A_{qs}^1 A_{q+1,s}^1 \delta_{q',q+2}\delta_{s's} + A_{q+1,s}^2 A_{qs}^1 \delta_{q'q}\delta_{s's}\right. \\
& \left. + A_{qs}^2 A_{q-1,s}^1 \delta_{q'q}\delta_{s's} + A_{q-1,s}^2 A_{qs}^2 \delta_{q'q-2}\delta_{s's}\right] \\
& + \frac{1}{4}\left[C_{qs}^1 C_{q+1,s-1}^1 \delta_{q',q+2}\delta_{s',s-2} + C_{qs}^1 C_{q+1,s-1}^2 \delta_{q'q}\delta_{s',s-2}\right. \\
& \left. + C_{qs}^2 C_{q-1,s-1}^1 \delta_{q'q}\delta_{s',s-2} + C_{qs}^2 C_{q-1,s-1}^2 \delta_{q-2,q'}\delta_{s',s-2}\right]
\end{aligned}
$$

To evaluate the gradient term $\nabla_{\boldsymbol{p}} Y_q^s \mathrm{d}\boldsymbol{p}$, we express the gradient operator $\nabla_{\boldsymbol{p}}$ in spherical coordinates on the unit sphere as $\nabla_{\boldsymbol{p}} = \frac{\hat{\theta}}{\sin\phi}\frac{\partial}{\partial\theta} + \hat{\phi}\frac{\partial}{\partial\phi}$, where

$$
\begin{aligned}
\hat{\theta} &= \{-\sin\theta, \cos\theta, 0\}, \\
\hat{\phi} &= \{\cos\theta\cos\phi, \sin\theta\cos\phi, -\sin\phi\}.
\end{aligned}
$$

Using the relation

$$
\frac{\partial Y_q^s}{\partial\phi} = \frac{1}{\sin\phi}\left\{q\cos\phi Y_q^s - \alpha_{qs} Y_{q-1}^s\right\},
$$

where α_{qs} is defined as

$$
\alpha_{qs} \equiv \left[\frac{(2q+1)(q^2-s^2)}{2q-1}\right]^{1/2},
$$

as well as the relations in table 1, we may write the projection of the gradient $\hat{\boldsymbol{z}}\cdot\nabla_{\boldsymbol{p}} Y_q^s$ as

$$
\hat{\boldsymbol{z}}\cdot\nabla_{\boldsymbol{p}} Y_q^s = -qA_{qs}^1 Y_{q+1}^s - \left(\alpha_{qs} - qA_{qs}^2\right) Y_{q-1}^s.
$$

Finally, the multipole harmonic relations in the table may be used to reduce the integral containing the gradient operator to an algebraic combination of A, B, C and α. The remaining terms that include integrals of $h(\boldsymbol{p})$ and Ψ are evaluated numerically after the arguments are reduced as much as possible.

Once the harmonic integrals are computed, (A 3) becomes a linear equation for the harmonic expansion coefficient $a_{q's'}$. Clearly, the equation is coupled to all other coefficients through the irreducible sums. However, for a finite truncation of the sums, we may write the set of equations (one for each coefficient) in the form of an eigenvalue equation $\boldsymbol{M}\cdot\boldsymbol{a}=\omega\boldsymbol{a}$, where $\boldsymbol{a}$ is a vector corresponding to all of the expansion coefficients and ω is one solution to the eigenvalue problem. Once $\boldsymbol{M}$ is computed for a finite number of harmonic modes (Q), a software package such as MATLAB is used to evaluate the eigenvalue set, $\{\omega^{(i)}\}$, which is a discrete approximation to the first $(Q+1)^2$ eigenvalues of (2.12).

REFERENCES

Banchio, A. J. & Brady, J. F. 2003 Accelerated Stokesian dynamics: Brownian motion. *J. Chem. Phys.* **118** (22), 10323–10332.

Butler, J. & Shaqfeh, E. S. G. 2002 Dynamic simulations of the inhomogeneous sedimentation of rigid fibers. *J. Fluid Mech.* **468**, 205–237.

Butler, J. & Shaqfeh, E. S. G. 2005 Brownian dynamics simulations of a flexible polymer chain which includes continuous resistance and multibody hydrodynamics interactions. *J. Chem. Phys.* **112** (014901), 1–11.

Chen, X. Q., Salto, T., Yamada, H. & Matsushige, K. 2001 Aligning single-wall carbon nanotubes with alternating-current electric field. *Appl. Phys. Lett.* **78** (23), 3714–3716.

Chwang, A. T. & Wu, T. Y. 1974 Hydromechanics of low-reynolds-number flow, part 2. Singularity method for stokes flows. *J. Fluid Mech.* **67** (4), 787–815.

Claeys, I. L. & Brady, J. F. 1989 Lubrication singularities of the grand resistance tensor for two arbitrary particles. *Physico Chem. Hydrodyn.* **11**, 261–293.

Essman, U., Perera, L., Berkowitz, M. L., Darden, T., Lee, H. & Pedersen, L. G. 1995 A smooth particle mesh ewald method. *J. Chem. Phys.* **103**, 8755.

Fair, M. C. & Anderson, J. L. 1989 Electrophoresis of nonuniformly charged ellipsoidal particles. *J. Colloid Interface Sci.* **127** (2), 388–400.

Fixman, M. 1986 Construction of Langevin forces in the simulation of hydrodynamic interaction. *Macromolecules* **19**, 1204–1207.

Han, S. P. & Yang, S. M. 1996 Orientation distribution and electrophoretic motions of rod-like particles in a capillary. *J. Colloid Interface Sci.* **177**, 132–142.

Harlen, O. G., Sundararajkumar, R. R. & Koch, D. L. 1999 Numerical simulation of a sphere settling through a suspension of neutrally buoyant fibers. *J. Fluid Mech.* **388**, 355–388.

Hasimoto, H. 1958 On the perioidic fundamental solutions of the Stokes equations and their application to viscous flow past a cubic array of spheres. *J. Fluid Mech.* **5**, 317–328.

Herzhaft, B. & Guazzelli, E. 1999 Experimental study of the sedimentation of dilute and semi-dilute suspensions of fibers. *J. Fluid Mech*. **384**, 133–158.

Kim, S. & Karrila, S. J. 1991 *Microhydrodynamics, Principles and Selected Applications*. Dover Publications.

Koch, D. L. & Shaqfeh, E. S. G. 1989 The instability of a dispersion of sedimenting spheroids. *J. Fluid Mech.* **209**, 521–542.

Larson, R. G. 1999 *The Structure and Rheology of Complex Fluids*. Oxford University Press.

Nicewater-Pena, S. R., Freeman, R. G., Reiss, B. D., He, L., Pena, D., Walton, I. D., Cromer, R., Keating, C. D. & Natan, M. J. 2001 Submicrometer metallic barcodes. *Science* **294**, 137–141.

Rose, K. A., Meier, J. A., Dougherty, G. M. & Santiago, J. G. 2007 Rotational electrophoresis of striped metallic microrods. *Phys. Rev.* E **75** (011503), 1–15.

Saintillan, D., Darve, E. & Shaqfeh, E. S. G. 2005 A smooth particle-mesh ewald algorithm for Stokes suspension simulations: the sedimentation of fibers. *Phys. Fluids* **17** (033301), 1–4.

Saintillan, D., Darve, E. & Shaqfeh, E. S. G. 2006*a* The growth of concentration fluctuations in dilute dispersions of orientable and deformable particles under sedimentation. *J. Fluid Mech.* **553**.

Saintillan, D., Shaqfeh, E. S. G. & Darve, E. 2006*b* Stabilization of a suspension of sedimenting rods by induced-charge electrophoresis. *Phys. Fluids* **18** (121701), 1–4.

Saintillan, D., Darve, E. & Shaqfeh, E. S. G. 2006*c* The effect of stratification on the wave number selection in the instability of sedimenting spheroids. *Phys. Fluids* **18** (121503).

Santillan, D., Darve, E. & Shaqfeh, E. S. G. 2006*d* Hydrodynamic interactions in the induced-charge electrophoresis of colloidal rod dispersions. *J. Fluid Mech.* **563** (223).

Saville, D. A. 1977 Electrokinetic effects with small particles. *Ann. Rev. Fluid Mech.* **9**, 321–337.

Smith, P., Nordquist, C., Jackson, T., Mayer, T., Martin, B., Mbindyo, J. & Mallouk, T. 2000 Electric-field assisted assembly and alignment of metallic nanowires. *Appl. Phys. Lett*. **77** (9), 1399–1401.

Squires, Todd M. & Bazant, Martin Z. 2004 Induced-charge electro-osmosis. *J. Fluid Mech.* **509**, 217–252.

Squires, Todd M. & Bazant, Martin Z. 2005 Breaking symmetries in induced-charge electro-osmosis and electrophoresis. *J. Fluid Mech.* **560**, 65–101.